Detection of inter band gap photoluminescence in multicrystalline silicon wafer

lena-marie jerpetjøn

Norwegian University of Life Sciences
Department of mathematical science and technology
Master thesis 30 credits 2011

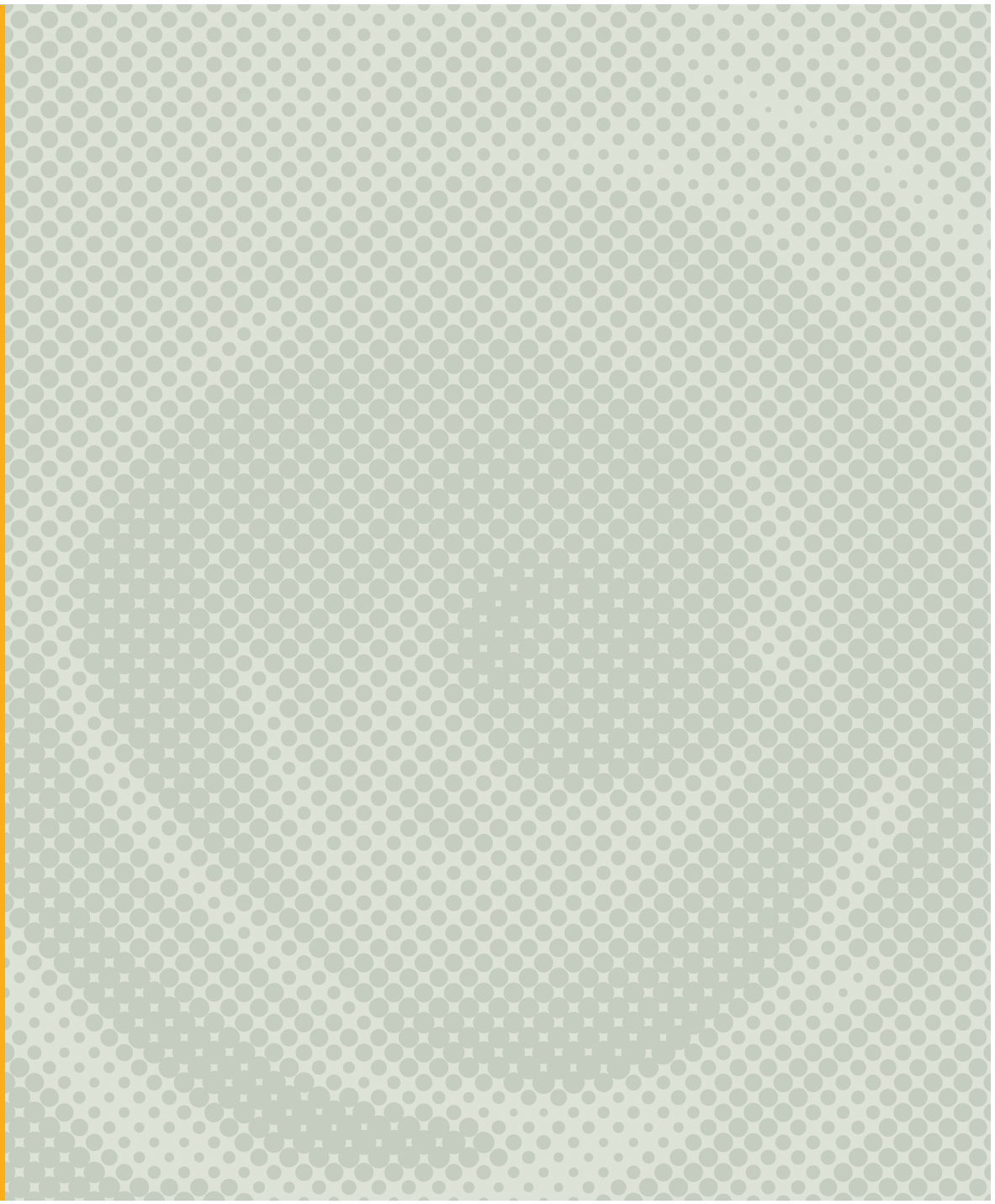

Preface

This master thesis represents the end of my studies in Renewable Energy and Environmental Physics at Norwegian University of Life Sciences (UMB), Department of Mathematical Science and Technology (IMT). This master thesis corresponds to 30 credits.

My choice of subject comes from my great interest in solar cell technology. My interest in this subject started with the solar cell technology course taught by Espen Olsen in the fall of 2009. This master thesis has made me even more interested in this particular field, and I have gained a valuable insight in this field.

I want to take this opportunity to thank my supervisor Espen Olsen and my co-supervisor Andreas Svarstad Flø for inspiring teamwork, encouragements and guidance. Also I want to thank Knut Kvaal for assisting me with image processing. In addition I want to thank Anicke Brandt-Kjelsen and Erik Gundersen for excellent guidance, support and proofreading. At last I want to thank the Department of Mathematical Science and Technology for lending me the equipment used in this thesis.

Ås, 12.05.2011

Lena-Marie Jerpetjøn

Abstract

Multicrystalline silicon wafers are attractive for the solar cell market due to low-cost production compared to monocrystalline silicon wafers, but the efficiency of multicrystalline silicon wafer is highly dependent on the quality of the material used. The large density of defects present in the material limits the quality of the multicrystalline silicon wafer. Typical defects in these multicrystalline wafers are dislocations, impurities and grain boundaries. Analyzing the presence of defects in the material is important to improve the quality of material for future photovoltaic applications. There are several different techniques invented and employed for defect characterization in multicrystalline silicon wafers. The technique used in this thesis was photoluminescence imaging. Photoluminescence imaging was performed by illuminating a multicrystalline silicon wafer with a laser and detect photoluminescence with a hyperspectral camera. The lifetime of carriers in the wafer was examined with the quasi-steady-state photoconductance technique to support the assumptions of high defect density in the wafer. The wafer was examined at two different temperatures, 300 and 93 Kelvin. Measurements executed at 300 K revealed photoluminescence solely from silicon. However, at 93 K the measurements revealed photoluminescence from both silicon and defects. The detected photoluminescence signal of silicon at 93 K was stronger though spectrally narrower than the signal detected at 300 K. The photoluminescence signal was affected by multi-phonon interactions. Two features, D_1 and D_2, were detected among other defects at 93 K. These two features have been put in relation to dislocation networks. Defect photoluminescence were detected at a lower energy range than photoluminescence from silicon. Defect photoluminescence were detected as point defects, grains, and large dislocation structures. Elements such as iron, nickel, copper, chromium and several others are assumed to give rise to the detected photoluminescence. Principal component analysis of the datasets recorded at 93 K and 300 K revealed the same spectral features of silicon and defects as the photoluminescence imaging technique. Inter band gap photoluminescence were detectable with the photoluminescence imaging technique employed when the wafer was frozen at 93 K. The technique for photoluminescence imaging has proven to be a fast and nondestructive way to detect inter band gap photoluminescence, caused by defects in multicrystalline wafers. This technique can be applied to analyze defects in wafers before constructing the finished solar cell to achieve a higher efficiency to be more attractive on the solar cell market.

Table of contents

Symbols

Symbols	Specifications
$f(E)$	Fermi-Dirac distribution
E_F	Fermi level
E_g	Energy band gap
E_C	Energy level of the conduction band
E_V	Energy level of the valence band
E_p	Photon energy
E_T	Trap energy level
N_V	Density of states in the valence band
N_A	Density of acceptor atoms
N_A^-	Density of ionized acceptor atoms
T	Absolute temperature
α	Temperature coefficient
β	Temperature offset
h	Plank's constant
c	Speed of light
λ	Wavelength
f	Frequency
n	Electron concentration
p	Hole concentration
Δn	Excess carrier concentration
n_i	Intrinsic carrier concentration
τ	Carrier lifetime
μ	Carrier mobility
D	Carrier diffusion
S	Surface recombination speed
U	Recombination rate
B	Radiative recombination coefficient
C	Auger coefficient
G	Generation rate
$\sigma_{n,p}$	Capture cross section
σ_c	Stefan-Boltzmann constant
σ	Conductance
N_t	Trap density
v_{th}	Thermal velocity
q	Charge
W	Width
X	Image array
t_A	Latent variables
p_A^T	Loading vector
E	Residual matrix

1. Introduction

The primary energy source today is fossil fuel. There are mainly three kinds of fossil fuel that our energy demands depend upon and those are coal, oil and natural gas. Fossil fuel provides a valuable service and it has brought the society to the economic level that it has today. The side effect of using fossil fuel is the release of greenhouse gases such as carbon dioxide (CO_2) to the environment, which contributes to an increase in global warming. Therefore, the world is in demand for increasing energy production from alternative energy such as solar, wind and moving water. Alternative energy simply means energy that is produced from sources other than our primary energy supply from fossil fuels. Increasing energy production from renewable energy and decreasing energy production from fossil fuels will immediately help to decrease the emission of greenhouse gasses. The first step to meet this goal is to improve the existing renewable technology and to invent new better solutions.

1.1 Solar Energy

The ultimate source of energy is the sun and its radiant energy is vital for life on this planet. The sun is essentially a hot sphere of gas heated by nuclear fusion reaction at its center. Hot bodies, such as the sun, emit electromagnetic radiation with a given wavelength or spectral distribution determined by the body's temperature. Planck's radiation law gives the spectral distribution of the emitted radiation. [1] Stefan Boltzmann Law is derived from Planck's radiation law and the total energy being emitted at all wavelengths by the blackbody is given by:

$$E = \sigma T^4 \tag{1.1}$$

Solar radiation can be harnessed and converted for human use by photovoltaic solar cells. The word photovoltaic has two parts: *photo* derived from the Greek word for light and *volt* relating to electricity pioneer Alessandro Volta. This literally means *light-electricity.* Photovoltaic cells are constructed of semiconductor material, most common material is silicon. Today, solar cells only contribute to a small amount to the world's energy needs. According to the European Photovoltaic Industry Association, solar power could provide energy for more than one billion people by 2020 and 26 % percent of global energy needs by 2040. [2]

1.2 Solar Cell Technology

Solar cells convert sunlight directly into electricity, by using the electronic properties of a semiconductor material. Silicon, as well as other semiconductor materials, comes in various forms, single-crystal, multi-crystal and amorphous. Solar cells depend upon the photovoltaic effect where photons interact with electrons in the semiconductor and create electron-hole pairs, known as carriers. Photons can be viewed upon as packages of energy and its magnitude is determined by their wavelength. The electron-hole pair eventually recombines with each other. The time from the generation to the recombination is referred to as carrier lifetime. The carrier lifetime depend upon the recombination mechanisms, some mechanisms has great impact on the efficiency of the solar cell.

"The higher the lifetime,
the better the solar cells
performance, all other
factor being equal" [3]

Multicrystalline silicon wafers have become increasingly important as precursor material for industrial solar cell production. Due to the fast production rate for cost reduction, the cause of thermal stress across the material result in an enhanced formation of dislocations. For further cost-reduction, less perfectly pure silicon feedstock material is used. Relatively high concentrations of transition metals impurities such as Fe, Ni, Cu and Cr are found in multicrystalline wafers, and they are believed to be a major limitation for the electronic properties of multicrystalline wafers. [4] Carrier lifetime in multicrystalline silicon wafers is low due to the large quantity of impurities and dislocations found in the material. They are detrimental to many silicon devices and limit the efficiency of multicrystalline solar cells. Therefore they are the major subjects of ongoing research. Photoluminescence spectroscopy is a promising technique for defect characterization.

The aim for my master thesis is to detect inter band gap photoluminescence in a multicrystalline silicon wafer by using a technique for photoluminescence imaging. The photoluminescence imaging technique is executed by illuminating the multicrystalline wafer with a laser and detecting photoluminescence with a hyperspectral camera. Inter band gap photoluminescence is investigated at two different temperatures for comparison.

2. Theoretical background

This chapter gives an overview over theory and terms used throughout this thesis. The literature described in this chapter is derived from relevant books and articles found in the reference list.

2.1 Silicon

Silicon (Si) is a light chemical element belonging to group IV in the periodic table. Being a tetravalent metalloid, the atom has 14 electrons in its shells. The two inner shells are full (2 and 8 electrons) while the outmost shell contains 4 electrons.

2.1.1 Silicon technology

In nature silicon combines with oxygen and other elements to form silicates. Silicon in the form of silicates constitute more than 25 % of the Earth's solid crust and that makes it the second most common element after oxygen. [5] Silica, silicon dioxide (SiO_2) is the major constituent in sand and is the main source material for extraction of silicon. [1] For silicon to be used as a semiconductor it needs to have high purity. Otherwise it is not capable of reaching high enough efficiency to be lucrative for the solar cell marked.

Production of multicrystalline silicon is a very cost effective method for producing crystalline silicon. The crucibles commonly used for production of multicrystalline silicon are mainly composed of fused silica, SiO_2. The melting of pure silicon with doping[1] atoms and solidification happens in the crucible and the resulting product is called an ingot. Impurities such as metals are introduced with the silicon feedstock before crystallization or within the crystallization process due to outdiffusion from crucible walls. [6] The ingot is cut into blocks using a horizontal band saw. Further, the blocks are cut into wafers using a wire saw.

2.1.2 Crystalline structure

The crystal structure of silicon is Face-Centered-Cubic diamond structure (FFC).
This structure has a unit cell of cubic geometry with atoms located at each corner and the centers of all cubic faces. [7]

[1] Doping atoms are impurity atoms introduced to alter the properties of the material.

Multicrystalline silicon, as most other crystalline solids, is composed of a collection of many small crystals or grains. They are formed when the solidification process approaches completion and the extremities of adjacent grains impinge one another. These grains are shaped with large irregularity. Boundaries that have two dimensions normally separate regions in the material that have different crystal structure or/and crystallographic orientations. These imperfections include stacking faults, grain boundaries and twin boundaries. Their concentrations and electrical activity could have a crucial effect on the solar cell efficiency. There exist some atomic mismatch within the region of the grain boundaries. The simplest of all defects are point defects, which are vacant lattice sites, normally in the form a missing atom. [7] The properties of the atomic arrangement of silicon are important in both design and operations of the solar cell.

2.2 Semiconductor Technology

2.2.1 Energy levels and Energy band

As mentioned in section 2.1 the two inner shells of silicon are full and do not interact with the surroundings. The outmost shell has four electrons that interacts with electrons from the nearest neighboring atoms to form covalent bonds[2]. [8] The silicon crystal can be viewed upon as a large number of atoms bonded together.

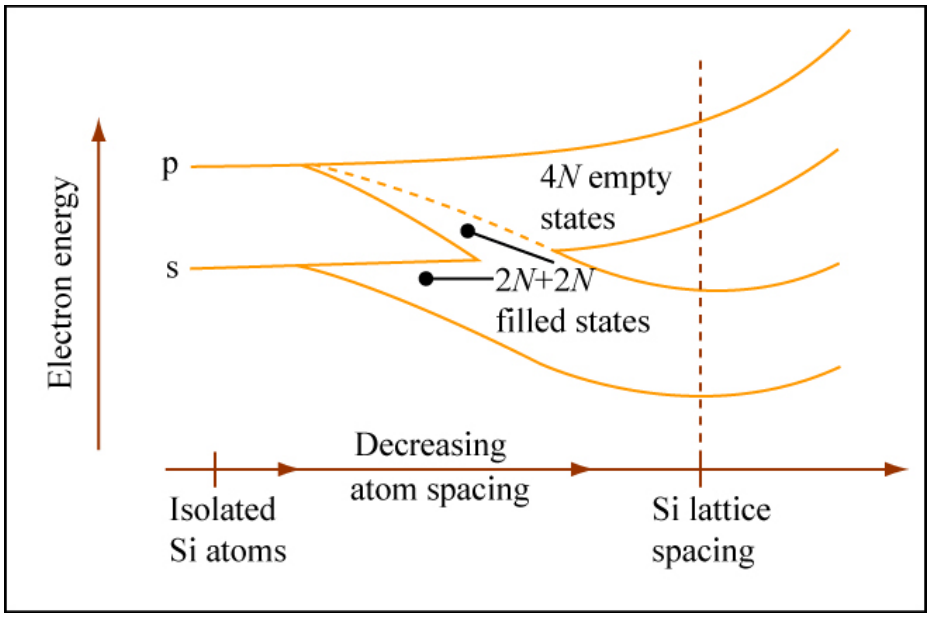

Figure 1: Allowed energies for electrons in an isolated atom and in a crystal. The distance between atoms decreases towards the right. [9]

[2] Covalent bond is the shearing of an electron pair between atoms.

Isolated atoms have a well-defined set of discrete energy levels available. If several atoms are brought closer together, as in a crystal, these energy levels will spread out into bands of allowed energy as illustrated in Fig. 1. Since each band contains a large number of available levels and these levels lie very close together, they can be viewed as a continuous range of energies available to electrons. Energy bands allowed for electrons are separated by a band gap, which is called the forbidden band gap. For a highly pure silicon semiconductor there are no energy levels available for electrons within the forbidden band gap. [1] For a semiconductor the band structure is characterized by a narrow forbidden band gap, which separates the valence band and conduction band. The width of this band gap is derived from [10]:

$$E_{gap} = E_C - E_V \tag{2.1}$$

where E_C and E_V is the energy level of the bottom of the conduction band and top of the valence band, respectively.

At zero temperature all allowed energy states in the valence band are completely occupied while all allowed energy states in the conduction band are completely empty. When the temperature increases, the number of thermally excited electrons across the forbidden band gap increases. The Fermi energy level refers to the energy of the highest occupied state in the system. The probability of occupation of allowed energy states of any given energy E in thermal equilibrium, when Pauli exclusion principle[3] is taken into account, is described by Fermi-Dirac distribution [10]:

$$f(E) = \left[1 + exp\left(\frac{E - E_F}{k_B T}\right)\right]^{-1} \tag{2.2}$$

where T is the absolute temperature, k_B is Boltzmann's constant and E_F is the Fermi energy level.

In intrinsic[4] semiconductors the Fermi level lies in the middle of the band gap with 50 % probability of occupation. For an extrinsic[5] semiconductor an expression for the position of the Fermi-level in a boron-doped semiconductor is given by:

$$E_F - E_V = k_B T ln\left(\frac{N_V}{N_A}\right) \tag{2.3}$$

[3] Pauli exclusion principle implies that each allowed state can be occupied by at most two electrons with opposite spin.
[4] Intrinsic meaning a pure undoped semiconductor.
[5] Extrinsic meaning a doped semiconductor, impurities intentionally introduced to the silicon crystal.

where N_V and N_A are effective densities of states in the valence band and the acceptor[6] densities, respectively. In an extrinsic semiconductor the position of the Fermi-level is directly determined by the doping concentration and temperature. The Fermi level in a boron-doped semiconductor moves towards the valence band-edge [10].

2.2.2 Temperature dependency of the band gap

The size of the forbidden band gap of silicon is temperature dependent and is given by the empirical equation [10]:

$$E_g(T) = E_g(0) - \frac{\alpha T^2}{T+\beta} \tag{2.5}$$

where T is the temperature in degrees kelvin, $E_g(0) = 1.17\ eV$ is the band gap in silicon at zero degrees kelvin, a temperature offset β = 636 K and a temperature coefficient α = 4,73x10^{-4} eV/K. The band gap of silicon decreases with increasing temperature as shown in Fig. 2. The temperature dependence of the band gap has been determined from the absorption edge [7]of silicon and is accurately described in a temperature range from 0 to 1000K. [10]

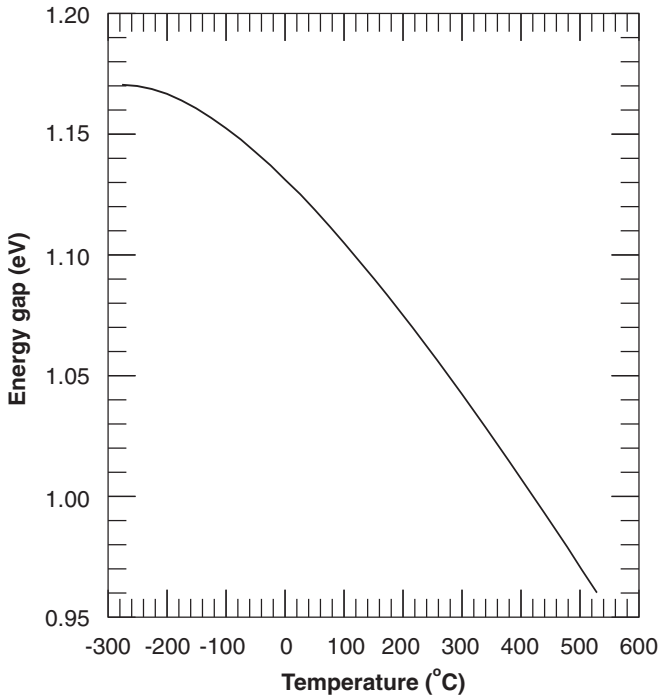

Figure 2: Silicon energy gap vs. temperature. The energy gap decreases with increasing temperature. [11]

[6] Acceptor atoms are atoms that only have three electrons in its outmost shell.
[7] Absorption edge represents the wavelength at which the element becomes ionized.

2.2.3 Electrons and Holes

Electrons in a covalent bond can be viewed upon as an electron in the valence band. A free electron is known to be in the conduction band. When an electron is exited into the conduction band it leaves behind a vacancy, broken covalent bond, known as a hole[8] in the valence band. The motion of electrons in the conduction band and holes in the valence band contributes the electrical current flow in a semiconductor. [1] Electrons and holes are known as carriers in a semiconductor.

For electron concentration n_0 in the conduction band and hole concentration p_0 in the valence band, in thermal equilibrium, the following expressions are given [10]:

$$n_0 = N_C exp\left(-\frac{E_C - E_F}{k_B T}\right) \tag{2.5}$$

$$p_0 = N_V exp\left(-\frac{E_F - E_V}{k_B T}\right) \tag{2.6}$$

where N_C and N_V are effective densities of states in the conduction band and valence band, respectively. Both n_0 and p_0 strongly depend upon the Fermi level and the temperature [10]. When the system is out of equilibrium, the number of electrons in the conduction band is denoted with the symbol n and the number of holes in the valence band with the symbol p.

2.2.4 Light Absorption and electron-hole pair generation

The fundamentals to the operation of solar cells are absorption of light to create electron-hole pairs. The process in which electron-hole pairs are created is referred to as generation. The direct excitation of an electron from the valence band to the conduction band is called *fundamental absorption*. Both sunlight and all electromagnetic radiation are composed of particles known as photons[9]. The amount of energy photons carries is determined by the spectral properties of their source. The photon energy and wavelength are related by the equation [12]:

$$E_\lambda = \frac{hc}{\lambda} \tag{2.7}$$

Where h is Plank's constant, λ is the given wavelength and c is the speed of light.

[8] Holes are regarded as physical particles with a positive charge. Electrons have a negative charge.
[9] Photons are elementary particles with high energy and low momentum.

Only photons with sufficient energy are capable of creating electron-hole pairs, which is those with energy grater than or the same as the energy band gap [12]. Some of the incoming photons will be reflected by the front surface and the rest will enter the bulk of the cell. The total energy and momentum of all particles involved in the absorption process must be conserved. The rate of light absorption is proportional to the intensity, the flux of photons, for a given wavelength. [1]

Light absorption in a direct-band-gap semiconductor

The absorption process for a direct-band-gap semiconductor is shown in the energy-momentum sketch of Fig 3. Every initial electron state in the valence band with energy E_1 and crystal momentum p_1 is associated with a final state in the conduction band at energy E_2 and crystal momentum p_2. [12]

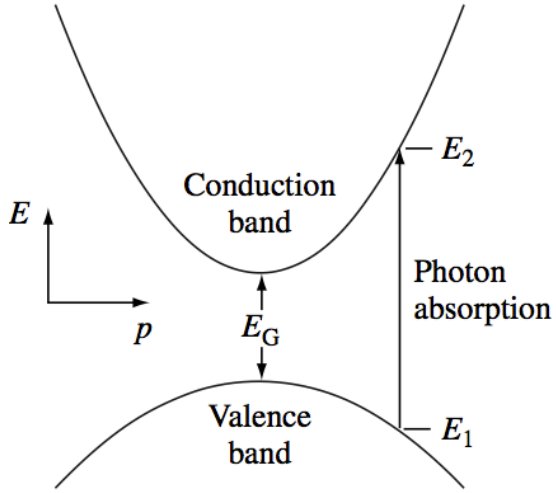

Figure 3: Phonon absorption in a direct band gap semiconductor for an incident photon with energy: $h\nu = E_2 - E_1 > E_g$. [12]

The electron momentum is conserved in the transition since p_1 equals p_2. The energy of the original photon equals the energy difference between the initial and final state [1]:

$$E_f - E_i = hf \tag{2.8}$$

where E_f and E_i is the energy of the conduction band and the valence band, respectively.

Light absorption in indirect-band-gap semiconductor

Silicon is an indirect-band-gap semiconductor. In indirect semiconductors the minimum energy in the conduction band and the maximum energy in the valence band occur at different values of the crystal momentum [12], as illustrated in Fig. 4. For direct

transition of electrons from the valence band to the conduction band, photon energies much larger than the forbidden band gap are required. However, transition can occur at lower energy levels by a two-step process. For the electron momentum conservation the photon absorption process involves an additional particle known as phonons[10]. In contrast to photons, phonons have low energy but relatively high momentum.

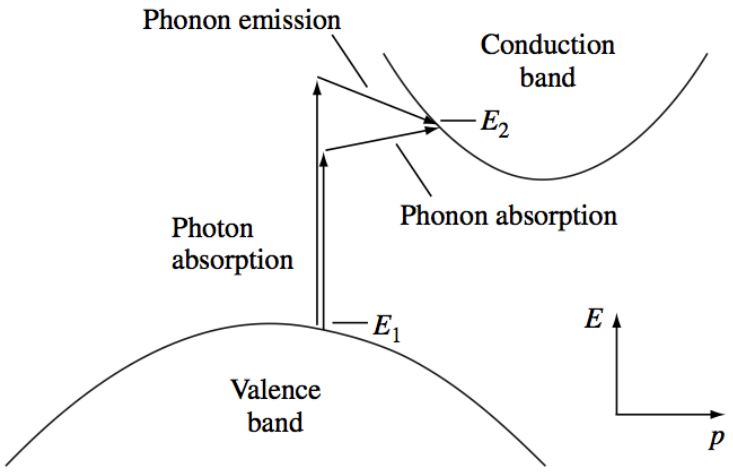

Figure 4: Phonon absorption in an indirect band gap semiconductor for an incident photon with energy: $h\nu > E_2 - E_1$. Energy and momentum in each case are conserved by the absorption and emission of a phonon, respectively. [12]

The minimum energy required to excite an electron from the valence band to the conduction band is [1]:

$$hf = E_g - E_p \tag{2.9}$$

where E_p is the energy of an absorbed phonon with the required momentum. Because of the requirement of an extra particle, the probability for light absorption is less in an indirect-band-gap semiconductor than for a direct-band-gap semiconductor. [1] As a result light penetrates more deeply into indirect band gap semiconductors than into direct band gap semiconductors. [12]

2.3 Carriers

Carriers in semiconductors are divided into majority carriers and minority carriers. In boron-doped semiconductors the majority carriers are holes and minority carriers are

[10] A phonon is just a quantum or a fundamental particle corresponding to the coordinated vibration of the crystal lattice.

electrons. The concentration of carriers in semiconductors depends upon different factors such as doping level, temperature, injection level and the amount of defects.

2.3.1 Law of mass action of carriers

In section 2.2.3 the expressions for the concentration of electrons in the conduction band and holes in the valence band were given by Eq. (2.5) and Eq. (2.6), respectively. Now, if they are multiplied together, a fundamental feature of carriers in a semiconductor is revealed, the equation becomes:

$$n_0 p_0 = N_C N_V exp\left(-\frac{E_g}{k_B T}\right) = n_i^2 \tag{2.10}$$

where n_i[11] is the intrinsic carrier concentration. In contrast to the carrier concentrations in equilibrium, their product (n_i^2) no longer depends on the Fermi-level and is doping independent. [10]

However, in the case of an extrinsic semiconductor the position of the Fermi level and thus the equilibrium concentrations n_0 and p_0 decisively depend upon the type and concentration of dopant used. Since this is a boron-doped semiconductor, the dopant is acceptor atoms denoted N_A. The law of mass action implies the separation of minority and majority carriers. The actual concentration of majority carriers and minority carriers are given by these two equations:

$$p_0 = N_A \tag{2.11}$$

$$n_0 = \frac{n_i^2}{N_A} \ll p_0 \tag{2.12}$$

2.3.2 Temperature dependency of carriers

The majority carrier concentration in an extrinsic semiconductor are regarded as temperature independent at 300 K, this assumption is invalid for much lower temperatures. [10] If electron density is measured as a function of temperature in a doped semiconductor, one observes three regimes as illustrated in Fig. 5. Temperature range from 0 K - 150 K is called the region of freeze-out, temperatures between 150 K –

[11] n_i is also the material parameter and it is temperature dependent, it increases with temperature.

500 K is referred to as saturation range and temperatures from 500 K and higher is called intrinsic range. [13] In the freeze-out range the fraction of ionized doping atoms is reduced due to the reduced energy available for thermal excitation ($p_0(T) < N_A$). At these temperatures the freeze-out of doping atoms, N_A, occurs and as a result the majority carrier concentrations decreases with decreasing temperature. In the saturation range the majority carrier concentration is assumed equal to the doping atoms concentration ($p_0(T) = N_A$). In the intrinsic range, the concentration of intrinsic carriers exceeds the doping concentration ($p_0(T) > N_A$). [10]

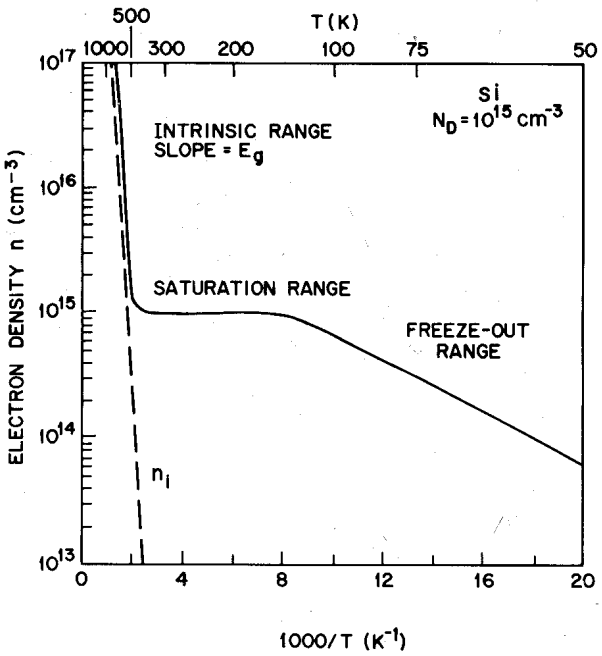

Figure 5: Electron density as a function of temperature for a silicon semiconductor with donor impurity concentration of 10^{15} cm^{-3}. [13]

To determine the precise value for the electron and hole concentration in a boron-doped semiconductor, the general approach starts from the fundamental condition of charge neutrality [10]:

$$n_0(T) + N_A^-(T) = p_0(T) \tag{2.13}$$

where N_A^- is the density of ionized[12] acceptor atoms, and is strongly temperature dependent. Acceptor atoms become ionized at low temperature due to the "freeze out" of carriers.

[12] Whenever an acceptor atom releases its extra hole to the valence band it becomes ionized.

Fig. 6 shows the ionization degree f_A[13] as a function of temperature for different doping concentrations.

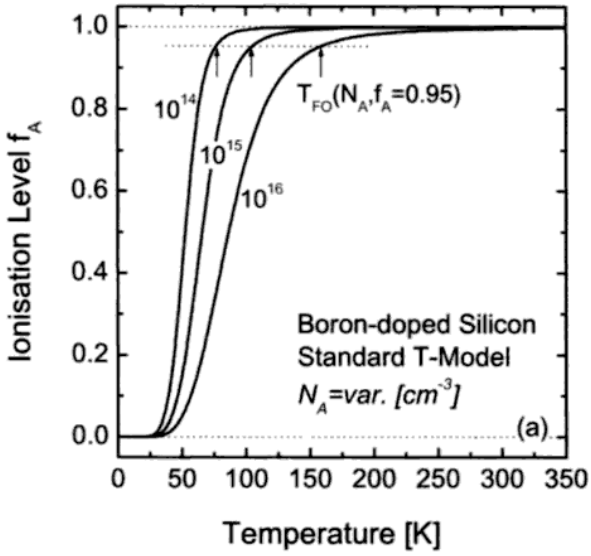

Figure 6: Ionization degree f_A of boron atoms in silicon as a function of temperature for different doping concentrations. [10]

The ionization degree is introduced to allow the magnitude of the "freeze-out" effect to be determined directly. The ionization degree equals the fraction of ionized acceptor atoms [10]:

$$f_A(T) = N_A^-(T)/N_A \tag{2.14}$$

Densities of non-ionized acceptor atoms is given by the expression [10]:

$$N_A^0(T) = \frac{N_A}{1+\frac{1}{2}exp\left(\frac{E_F-E_A}{k_BT}\right)} \tag{2.15}$$

where E_A is the energy level of the acceptor atoms within the band gap.

In more highly doped materials the freeze-out of doping atoms occur at higher temperatures. This is an effect of the reduced distance between the doping level and the Fermi-level, which results in reduction of ionization of the doping atoms. In boron-doped material the general temperature dependence of the majority carrier concentrations, for T< 623 K, is given by the equation [10]:

$$p_0(T) = f_A(T)N_A \tag{2.16}$$

[13] The ionization degree f_A ranges from 0 to1.

2.3.3 Carrier mobility

Electron mobility μ in a crystal depends on the temperature, the doping concentration and upon the crystalline direction in which they move. In boron-doped silicon semiconductors the major elements affecting the electron mobility are scattering of carriers from phonon (lattice vibrations) and carrier scattering from acceptor atoms, also known as impurity atoms. [14]

The approximate relationship between the phonon limited electron mobility and the temperature is: [15]

$$\mu_L \propto T^{-3/2} \tag{2.17}$$

Impurity scattering is most efficient when the impurities are ionized. The temperature dependency of the impurity scattering is given by:

$$\mu_I \propto \frac{T^{3/2}}{N_I} \tag{2.18}$$

where N_I is the density of ionized dopant atoms.

2.4 Carrier lifetime in crystalline silicon

The excitation of an electron from the valence band to the conduction band can appear from both thermal processes and from the absorptions of photons. The inverse process is when an electron relaxes back from the conduction band to the valence band, where it interacts with a hole. This process is referred to as the recombination process. The excess energy and the change in momentum are either released as photons or phonons or transferred to other carriers. This ensures energy and momentum conservation. [10] The lifetime of electron-hole pairs is also referred to as recombination lifetime and they commonly exhibit lifetimes between 1 μs to a few milliseconds [3]. The effective recombination lifetime consists of several independent recombination processes that can occur simultaneously. The term apparent lifetimes is used for cases where the measured quantity does not actually represent recombination but a result of distortion caused by trapping[14] effects in multicrystalline silicon. [16]

[14] Trapping refers to the situation when an electron is captured in a state within the band gap before recombining with a hole in the valence band.

The density of excess carriers Δn depends on the minority carrier lifetime τ and the net recombination rate U. In general, recombination lifetime is given by [16]:

$$\tau = \frac{\Delta n}{U} \tag{2.19}$$

where $\Delta n = \Delta p$ is the excess carrier density when there is no traps present.

2.4.1 Carrier recombination mechanisms

In semiconductors there are three fundamental recombination mechanisms. These are radiative, Auger and Shockley-Read-Hall recombination. They are illustrated in Fig.7.

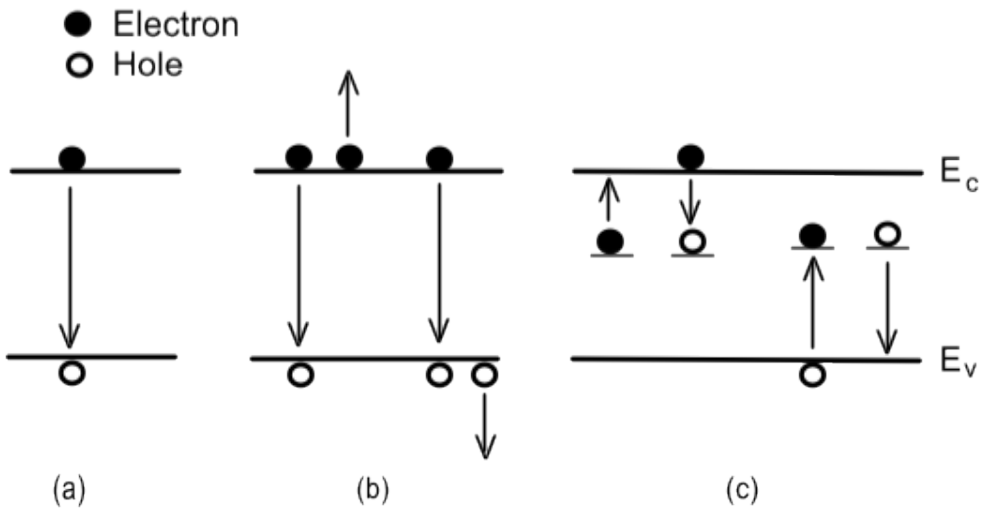

Figure 7: Recombination processes in semiconductors: a) Radiative band-to-band recombination, b) Auger recombination and c) Shockley-Read-Hall recombination.

All three mechanisms can occur either from band-edge to band-edge or via intermediate level in the band gap. Band-to-band recombination occurs principally through Auger and radiative recombination processes. Shockley-Read-Hall recombination is also called multi-phonon [15] recombination [16]. The multi-phonon process dominates recombination through the intermediate levels.

A common classification of the different recombination mechanisms distinguishes intrinsic and extrinsic mechanisms. *Intrinsic recombination mechanisms* are always present either as radiative recombination where the excess energy is released as a photon or Auger recombination where the excess energy is transferred to a third carrier, the transition thus being non-radiative, or both. Phonons may also be involved

[15] Multi-phonon refers to the process where an electron interacts with several phonons in the lattice.

in both processes, to ensure momentum conservation. Shockley-Read-Hall recombination is the *extrinsic recombination mechanism,* which is explained by a stepwise process where the electron transition occurs via defects that introduce intermediate energy level within the band gap. [10]

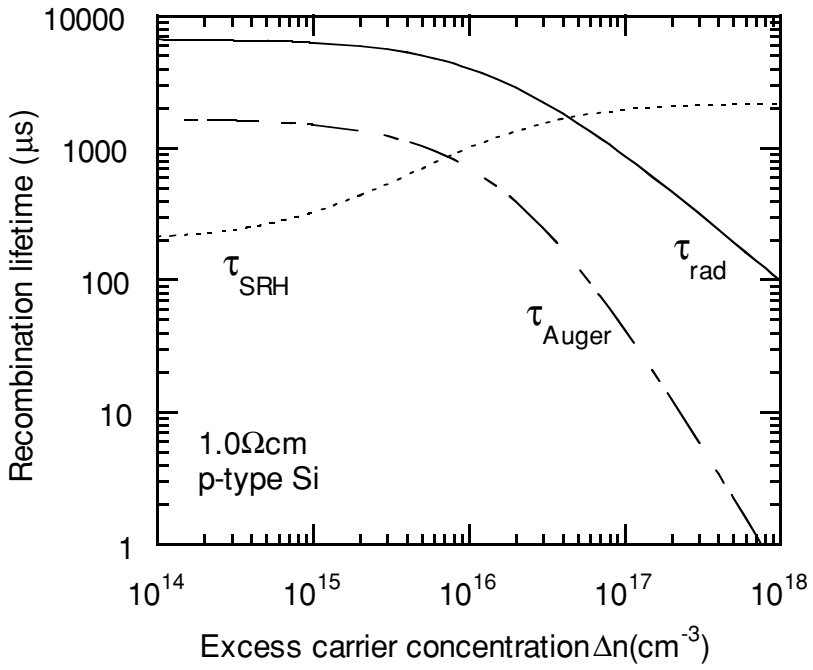

Figure 8: Effective lifetime made up of SRH, radiative and Auger terms. Each of these mechanisms dominates in turn as the excess carrier density increases. [16]

The recombination lifetime of the three mechanisms varies due to the increase of carrier concentrations. As illustrated in Fig. 8 both radiative and auger recombination lifetimes dominate at high carrier concentrations, while Shockley-Read-Hall recombination dominates at low carrier concentrations. How the different mechanisms depend on the excess carrier concentrations is further explained in the next sections.

2.4.2 Radiative recombination

Radiative recombination is the reverse of the optical absorption process, direct annihilation of an electron-hole pair. The process involves emission of a photon with energy approximately equal to the forbidden-band-gap, since thermalisation ensures that any initial excess carrier energy is lost well before the recombination occurs. A second absorption of the emitted photon may occur before it leaves the crystal. Since both electrons and holes are required for the process to occur the radiative

recombination rate, U_{rad}, depends on both their concentrations. In boron-doped material this gives rise to the following expression [16]:

$$U_{rad} = B\Delta n(N_A - \Delta n) \tag{2.20}$$

where B is a constant and the equilibrium electron concentration for boron-doped material has been neglected. From Eq. (2.19), the general expression for the radiative recombination lifetime τ_{rad} is given by [16]:

$$\tau_{rad} = \frac{1}{B(N_A+\Delta n)} \tag{2.21}$$

Radiative recombination is typically the dominant recombination process in direct semiconductors. Because of the phonon emission or absorption requirements in indirect semiconductors for energy and momentum conservation, the radiative process could be negligible compared to other recombination mechanism. [16] The radiative recombination coefficient B is temperature dependent and it decreases with increasing temperature. Its temperature dependency is shown in Table 1.

Table 1: Temperature dependent excess carrier concentration and radiative recombination coefficient. [17]

Temperature (K)	Δn (cm^{-3})	B(T) (cm^3/s)
77	$1.95x10^{-20}$	$8.01x10^{-14}$
90	$8.87x10^{-15}$	$4.57x10^{-14}$
112	$3.69x10^{-8}$	$2.14x10^{-14}$
300	$9.97x10^{9}$	$4.73x10^{-15}$

It is clear from the Table 1 that B is larger for low temperatures. As shown in Fig. 8 At least one of the other recombination mechanisms will be dominant over the radiative process at any given excess carrier concentration, Δn.

2.4.3 Auger recombination

Auger recombination involves a three-particle interaction where the excess energy released by the recombination of an electron-hole pair is transferred to a third free carrier. The third free carrier releases its excess energy as phonons to the crystal, a process known as thermalisation. [10, 16] The third free carrier is either an electron in the conduction band or a hole in the valence band [1].

Depending on the carrier type, the Auger recombination rate, U_{Auger}, is proportional to the electron-electron-hole process (n^2p) and the electron-hole-hole process (p^2n). The net recombination rate is given by [10]:

$$U_{Auger} = C_n(n^2p - n_0^2p_0) + C_p(np^2 - n_0p_0^2) \quad (2.22)$$

where C_n and C_p are the Auger coefficient for the electron-electron-hole process and the electron-hole-hole process, respectively.

Auger recombination lifetime is injection[16] dependent and at low-injection conditions Auger lifetime for boron-doped silicon is given by [10]:

$$\tau_{Auger} = \frac{1}{C_pN_A^2} \quad (2.23)$$

Under high injection conditions both electrons and holes are available to act as the third free carrier, and the relevant expression is [10]:

$$\tau_{Auger} = \frac{1}{C_a\Delta n^2} \quad (2.24)$$

where $C_a=1.66\times10^{-30}cm^{-6}s^{-1}$ which is the so-called ambipolar Auger coefficient, $C_a=C_n+C_p$.

Ideally, Auger recombination lifetime depends on the inverse square of the carrier density $\left(\tau_{Auger} \propto \frac{1}{\Delta n^2}\right)$. Therefore Auger lifetime decreases as the excess carrier concentration increases. Auger recombination dominates the radiative recombination under high-level injections. [10] At lower excess carrier concentration, in all but the best material with the best surface passivation, the lifetime is actually dominated by recombination through defects. [16]

2.4.4 Shockley-Read-Hall recombination

Shockley-Read-hall recombination is recombination through defects in the bulk of the semiconductor. Defects from impurities and crystallographic imperfections produce discrete energy levels within the forbidden band gap. Defect levels, centres, can be occupied either by electrons or holes. [10] They can also act as traps, or solely as traps. In this case a captured carrier is subsequently injected back into the band from which it

[16] Injection level determines the excess carrier concentration Δn.

came. Trapping causes a change in free carrier concentrations that can impact the overall carrier dynamics. Trapping does not contribute directly to recombination. [16]

For a semiconductor with a trap density, N_t, with each trap having a single energy level E_t within the band gap the probability of an electron occupying the energy level for any trap is given by [14]:

$$\mathcal{F}_1 = \left[1 + exp\left(\frac{E_T - E_F}{k_B T}\right)\right]^{-1} \tag{2.25}$$

The result of the net recombination-generation rate by traps, U_T, can be written [1]:

$$U_T = \frac{np - n_i^2}{\tau_{p0}(n + n_1) + \tau_{n0}(p + p_1)} \tag{2.26}$$

where τ_{n0} and τ_{p0} are lifetime parameters, also known as fundamental electron and hole lifetime. Their value depend on the carrier thermal velocity v_{th}, the density of recombination centres and the capture cross-sections σ_n and σ_p of the given centre [16]:

$$\tau_{p0} = \frac{1}{N v_{th} \sigma_p} \tag{2.27}$$

$$\tau_{n0} = \frac{1}{N v_{th} \sigma_n} \tag{2.28}$$

The lifetime parameters depend upon the type of trap and the volume density of trapping defects. Since the recombination rate depend upon the energy level of a given trap, E_T, the parameters n_1 and n_2 are introduced. [1] These parameters are the electron and hole densities when the Fermi level merges the energy level of the trap. [16]

$$n_1 = N_C exp\left(\frac{E_T - E_C}{k_B T}\right) \tag{2.29}$$

$$p_2 = N_V exp\left(\frac{E_C - E_G - E_T}{k_B T}\right) \tag{2.30}$$

$$n_1 p_1 = n_i^2 \tag{2.31}$$

where N_C and N_V are the effective densities of states at the conduction and valence band edges, and E_C and E_G are the conduction band and the band-gap energies. [16]

If τ_{n0} and τ_{h0} are of the same order of magnitude, then U will have its peak value when $n_1 \approx p_1$. This occurs if the defect levels lies near the middle of the forbidden band gap.

Therefore, impurities that introduce energy levels near mid gap are very effective recombination centres. [1] Shockley-Read-Hall recombination are dependent on the excess carrier concentration since the capture cross sections are strongly injection dependent. Since the electron and hole lifetime reflects the value of the capture cross-section, the lifetime is injection dependent. As shown in Fig. 8, Shockley-Read-Hall dominates at low excess carrier concentrations. [16]

2.4.5 Surface recombination

The surface of silicon substrate represents an abrupt discontinuity in the crystal structure, which leads to a large quantity of partially bonded atoms. These dangling bonds give rise to recombination active defect levels within the band gap near the surface of the semiconductor. [10] This is why surface recombination is a special case of SRH recombination. However, unlike bulk Shockley-Read-Hall centres, these states do not usually occupy a single energy level, but rather form a set of states distributed across the band-gap. [16]

For simplicity, the surface recombination rate, U_S, in a boron-doped semiconductor is generally written [12]:

$$U_S = S_n(n - n_0) \tag{2.32}$$

where S_n is the effective surface recombination velocity.

The fundamental process for reducing the surface recombination rate is passivation of the semiconductors surface. This will remove the "dangling bonds" from the surface.

2.4.6 Total recombination lifetime

The four recombination mechanisms can occur simultaneously. For each independent process the overall recombination rate is the sum of the individual recombination rates, resulting in an effective lifetime τ_{eff} given by [16]:

$$\frac{1}{\tau_{eff}} = \left(\frac{1}{\tau_{SRH}} + \frac{1}{\tau_{Auger}} + \frac{1}{rad}\right) + \frac{1}{\tau_{surface}} = \frac{1}{\tau_{SRH}} + \frac{1}{\tau_{Auger}} + \frac{1}{rad} \tag{2.33}$$

Since the surface of the wafer is passivated the surface recombination term in the equation can be neglected.

The recombination rate depends non-linearly on the change in carrier densities from their equilibrium values. Thus, the total recombination lifetime is given by [18]:

$$\tau_T = \left(\frac{1}{\tau_{SRH}} + \frac{1}{\tau_{Auger}} + \frac{1}{\tau_{Rad}}\right)^{-1} \tag{2.34}$$

At higher carrier densities the lifetime in silicon is controlled by Auger recombination and at low carrier densities by Shockley-Read-Hall recombination. Radiative recombination is normally negligible.

2.5 Defects centres in the band gap

The short carrier lifetime in silicon semiconductors can be viewed as a loss mechanism in solar cells. Short carrier lifetime reduces the overall efficiency of the solar cell. Defects will affect the carrier lifetime, as explained in section 2.4.4, by acting as active recombination states in the otherwise forbidden band gap. Defect such as impurity atoms can be incorporated in the silicon crystal structure in two ways. They can occupy positions squeezed in between the atoms of the host crystal, in which case they are known as *interstitial impurities*. They can also substitute for an host atom in the crystal while maintaining the regular atomic arrangement in the crystal structure, in which case they are know as *substitutional impurities*. Impurities can also exist in complex with other elements or as precipitates. [1]

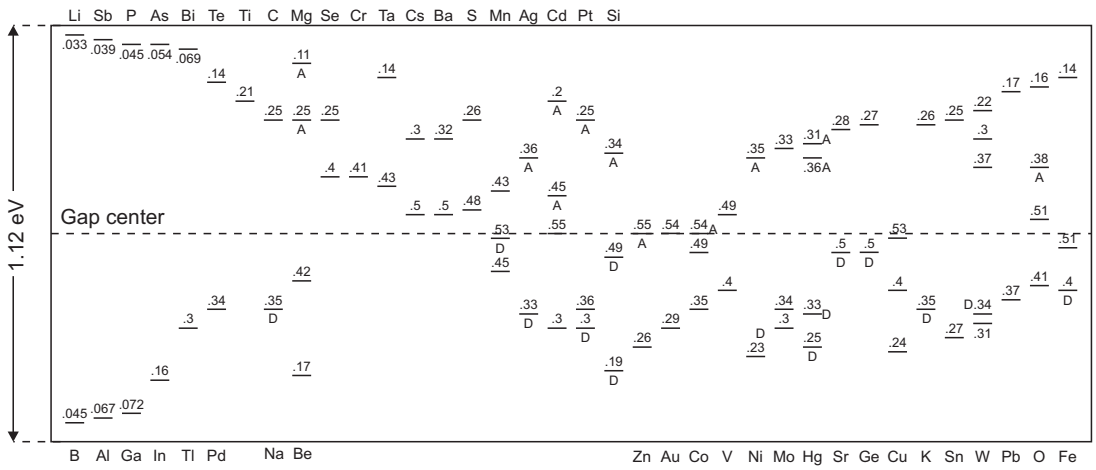

Figure 9: Energy levels within the band gap introduced by impurities in the silicon crystal. There are both acceptor atoms and donor atoms. [11]

Some impurities introduce multiple allowed energy levels within the forbidden band gap. Crystal defects act in a similar way to introduce levels into the forbidden band gap. Impurities, particular those which introduce energy levels near the middle of the band gap, generally degrade the properties of the semiconductor. The essence is that the probability for recombination decreases with increasing difference in energy for the electron-hole pairs. States introduced within the band gap decreases this difference in energy and thereby leads to higher recombination rates and shorter lifetime for the minority carriers. The traps or allowed states are said to be shallow or deep. Electrons have higher mobility then holes and are therefore more easily trapped by these states. [8]

2.5.1 Doping

To alter the properties of the semiconductor, doping atoms also known as impurity atoms are intentionally introduced to the silicon crystal. Doping atoms decrease resistivity in the material due to change in carrier densities. The element, from the periodic table, that the semiconductor is doped with is chosen for its properties. There are two common doping elements in silicon and they are from group V and III in the periodic table. Group V is tetravalent, having 5 electrons in its outmost shell. Group III is trivalent, having 3 electrons in its outmost shell. In general, dopants will give rise to shallow energy levels close to the band edges. Boron is a trivalent element and as mentioned earlier are called acceptor atoms. The silicon crystal is intentionally contaminated with boron because of its diffusion rate into the crystal and because it introduces an energy level of 0.045 eV from the valence band edge inside the band gap of silicon. If the semiconductor were doped with a tetravalent elements they would in the same way as for trivalent introduce energy levels within the band gap. Thus, introduce an energy level just below the conduction band edge and function as a donor of its extra electron that is noncontributing in any covalent bonding. The wafer is doped with both trivalent and tetravalent elements to create a depletion layer within the wafer for the operating of the solar cell.

2.5.2 Transition metals

Impurities non-intentionally introduced in the silicon crystal appear mainly from the casting of the silicon ingots. Impurities are usually incorporated in the silicon crystal as interstitial point defects. [7] These impurities give rise to energy level within the band

gap. The possibility for the electron-hole pair to recombine is largest when the empty electronic states are near the middle of the band gap. Elements with deep levels above the middle of the band gap will in general be more active than elements with deep levels below the middle of the band gap. Some of the elements found in silicon are iron, nickel, copper, manganese, oxygen or chromium. Those elements that introduce deep levels are most detrimental to the efficiency of the solar cell. [8]

The main impurities found in silicon semiconductors during device fabrications belong to the 3d transition-metals group. The transition metals are characterized by an increasing number of electrons in the shell with increasing atomic number. Transition metals dissolved in silicon are electrically active and exhibit deep energy levels, which acts as donor or as acceptor states. 3d transition metals are metastable and they tend to form complexes and pairs with other elements to achieve a more stable form in the silicon lattice. Impurity concentrations rarely exceeds $10^{13}\,cm^{-3}$, the main impurities in processed silicon wafers are iron, copper and nickel. Dissolved impurities with high minority-carrier capture cross-section causes a drastic reduction of minority carrier lifetime in silicon. [19]

Large quantities of iron impurities are found in multicrystalline silicon wafers, they are introduced to the silicon crystal through the crucible walls. Iron is a metal in the first transition series in the periodic table. In block cast multicrystalline silicon it is typically found that most iron is attached to crystallographic defects such as dislocation or grain boundaries. Most iron is shown to be less effective recombination centres than isolated interstitial iron (Fe_i). In regions with low crystallographic defect densities, interstitial iron largely limits the recombination lifetime in multicrystalline silicon. [20]

In boron-doped silicon, the interstitial positively charged Fe_i forms iron-boron pairs, Fe_iB_s, with the negatively charged substitution boron B_s atoms in equilibrium. These pairs can be separated by energy supply such as illumination. [20] The isolated and paired form of interstitial iron has considerably different recombination properties. This leads to significant changes in minority lifetime and diffusion length after iron-boron pair separation. [21] Iron-boron pairs exhibit donor levels with activation energies between 0.1 and 0.2 eV from the valence-band edges. [19]

2.5.3 Crystal defects

Crystal defect such as grain boundaries and dislocations are areas where transition metals tend to precipitate. Grain boundaries are more electrically reactive than the gains themselves and because of their higher energy state impurities segregate along them. The recombination activity of dislocations varies strongly with their physical properties. [22] Twin boundaries are a special type of grain boundaries in areas of the wafer where there is specific mirror lattice symmetry. Atoms on one side of the boundary are located in the mirror image position of the other side. Twin boundary describes the region of material between these boundaries. In silicon crystals they are formed from annihilating heat treatment. [7]

Dislocation clusters form small angle grain boundaries, they are crystal defect that clump together. [23] They form extended defected regions that remain separated from each other. Defect clustering occurs during crystal growth when local thermal stress exceeds yield stress of some preferred grain orientations, causing stress relief through local generation of defect networks. Defect clusters also serve as internal gettering sites for metallic impurities, and it often result in impurity precipitation at these sites. [24]

2.6 Carrier lifetime measurements

An accurate determination of recombination lifetime is a fundamental condition for lifetime spectroscopy. [10] Measurements of minority carrier lifetime in silicon are extremely valuable for process control and device optimization, as well as for material device research. The carrier lifetime measurement is based on the recombination dynamics of excess carriers. Excess carriers are normally generated optically. [10]

Photoconductance monitors the result of the decay of carriers back to their equilibrium. If traps are assumed absent, $\Delta n = \Delta p$, the net excess conductance $\Delta\sigma$ is given by [16]:

$$\Delta\sigma = q\Delta n(\mu_n + \mu_p)W \tag{2.32}$$

where W is the width of the sample, μ_n and μ_p are the mobility of electrons and holes, respectively.

A generalized analysis procedure has been proposed by Nagel et al. in order to define an effective lifetime regardless of the decay time of the illumination source [16]:

$$\tau_{eff} = \frac{\Delta n_{av}}{G_{av}(t) - \frac{\partial \Delta n_{av}(t)}{\partial t}} \tag{2.33}$$

where n_{av} is the average excess carrier density and G_{av} is the average generation rate, both calculated over the whole wafer thickness.

2.6.1 Quasi-steady-state photoconductance (QSSPC) technique

Quasi-steady-state photoconductance technique is used for lifetime measurements in semiconductor materials. A photographic flash lamp is used as the generation source. The wafer is inductively coupled by a coil to radio-frequency-bridge[17], which senses change in the permeability of the wafer and therefore its conductance. A reference cell is used to determine the time dependence of both the excess photoconductance of the wafer $\Delta\sigma(t)$ and its illumination $I(t)$, by using appropriate calibration functions. [10] The reference cell is located inside the apparatus.

The illumination intensity of the generation source is slowly reducing to zero over several milliseconds. The decay has to be long enough to ensure that the sample remains in steady state, in terms of the recombination process. The effective lifetime for quasi-steady-state case is calculated via the expression [16]:

$$\tau_{eff} = \frac{\Delta n_{av}}{G_e} \tag{2.34}$$

where G_e is the generation rate produced by the incident light.

The apparent carrier lifetime τ_{app} is calculated from the excess conductivity and the photo-generation rate with the assumption that $\Delta n = \Delta p$:

$$\tau_{app} = \frac{\Delta\sigma}{G_e(\mu_n + \mu_p)} \tag{2.35}$$

The apparent lifetime is affected by the density of traps in the semiconductor.

[17] Radio-frequency- bridge is used to measure electrical properties in a material. The impedance is measured.

2.7 Photoluminescence

The definition of photoluminescence is the spontaneous emission of light from a material under optical excitation. The excitation energy and intensity are chosen to examine different regions and excitation concentrations in the wafer. Investigation of photoluminescence can be used to characterize a variety of material parameters. Features of the emission spectrum can be used to identify surface, interface and impurity levels within the band gap of silicon. The intensity of the photoluminescence signal provides information on the quality of the surfaces and interfaces. [25] The photoluminescence technique allows characterization of a material without preparation of contacts, and gives information about the existing radiative defects. [26]

2.7.1 Temperature dependent photoluminescence

The temperature dependence of photoluminescence in most semiconductors is mainly because of the strong temperature dependence of the non-radiative routes, the band-to-band radiative route is fairly temperature independent. [27] Thermally activated processes cause change in photoluminescence intensity with temperature. When the temperature is sufficient low states within the band gap become radiative active. If carriers recombine radiatively through these states, the energy of the emitted light can be analyzed to determine the energy of the defect or impurity level. An important feature is that the temperature has to be low enough to discourage thermal activation of carriers out of the traps. When intermediate states have radiative levels, they are identified in the photoluminescence spectrum. [25]

2.8 Multivariate statistical analysis

Large datasets can be analyzed by using multivariate image analysis. The goal of multivariate image analysis methods is to extract significant information from an image dataset while reducing its dimensionality. [28] Dimension reduction is the process of reducing the number of bands of a hyperspectral image. It maps dimensional data into a lower dimension while preserving the main features of the original data. Principal component analysis is the workhorse of multivariate image analysis. The key is the proper reorganization of the original 3-way array. An image that is I by J pixels with k spectral bands are reshaped to form a 2-way array that is IJ by k. Principal component analysis can be performed on the 2-way array. Mean centering is typical used in this kind of analysis. [29]

The multivariate images are produced from data collected in multi spectral bands. The multivariate image consists of a stack of congruent images where each image is measured for a different wavelength and energy. [30] Since multivariate images consist of several congruent images, each vector in such an image consists of highly correlated pixel [18] intensities. Principal component analysis transforms large datasets into a number of uncorrelated principal components or scores. [28]

Mathematically, principal component analysis performs a decomposition of the covariance structure that exist within the original data matrix X. This makes it possible to visualize and interpret the underlying source of variations that are present in the data. The principal component analysis model of $X(n\times k)$ is given:

$$X = t_1 P_1^T + t_2 P_2^T + k t_A P_A^T + E \tag{2.36}$$

where the $t_i P_i^T$ products represents independent sources of variation that exist within the data matrix X. The $t's(n\times 1)$ are the principal components, scores defined as linear combination of the original variables in X. These linear combinations are defined by the weight vectors $P_i(k\times 1)$, commonly known as loading vectors. The element of the weight vectors $(P_i, i = 1,2, \dots\dots, A)$ are computed to maximize the amount of explained variance of the data matrix X. Since the principal components are constrained to be orthogonal, the amount of explained variance by each principal component is in decreasing order. The number of principal components, A, of the model, is chosen such that most of the structured information in X is modeled while leaving the unstructured information, or noise, in the residual matrix E. [31]

[18] Each pixel has a hyperspectral signature that represents different materials.

3. Experimental

3.1 Background

The low efficiency of today's solar cells is a challenge for the solar cell marked. The reason for the low efficiency of multicrystalline silicon wafers is their significant amount of defects in the material. Defects such as grain boundaries, dislocations and point defects cause the minority carrier lifetime to decrease. The efficiency of solar cell can be improved by extending the carrier lifetime. Impurities that exist as point defects or segregate along grain boundaries are the most detrimental defects in wafers. The understanding of how impurities diffuse into the material under production of silicon wafer and where they are located in the final result is decisive for the future of photovoltaic systems based on multicrystalline silicon wafers. The goal for this thesis is to use a photoluminescence mapping technique for detection and characterization of defects in the wafer by using a laser and a hyperspectral camera.

3.2 Material and Equipment

This chapter deals with the equipment used in this thesis, and how they were applied. It is important to explain how the experiment was executed to understand the results and discussion.

3.2.1 MC-Si Wafer

The multicrystalline silicon wafer examined in this thesis was produced from a block cast in a crucible composed of fused silica and doped with boron. The dopant concentration is approximately 10^{16} cm^{-3}, which is far less than the concentration of host atoms (silicon) 10^{23} cm^{-3} in the lattice. The impurity concentration is less than the dopant concentration, approximately 10^{12} cm^{-3}. Since the surface of the wafer is passivated, surface recombination mechanism can be neglected. It is assumed that the wafer contains a large amount of dislocations due to problems with the crystallization process during the production. An image of the wafer examined in this thesis is illustrated in Fig.10. Histogram stretching is used on Fig.10 to enhance the contrast in the wafer structure. This particular wafer was chosen for investigation in this thesis because of its many faults such as high dislocation and impurity density.

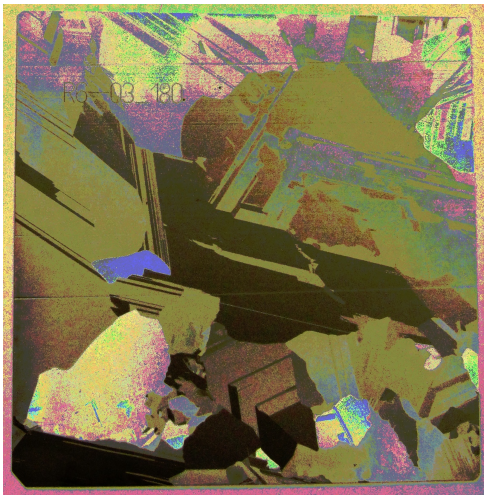

Figure 10: The multicrystalline silicon wafer examined in this thesis.

3.2.2 Camera and software

The camera used in this thesis is a hyperspectral camera with appellation *"HySpex SWIR-320i"*. The hyperspectral camera records photons with different wavelength at the same time. This camera records electromagnetic radiation with spectral wavelength from 935 nm to 1700 nm. This specter is divided into 150 bands, each with a width of 5 nm. Each band and their corresponding energy and wavelength is found in Table 2.

Hyperspectral imaging (imaging spectroscopy) combines the power of digital imaging and spectroscopy. For each pixel in an image, the hyperspectral camera detects the light intensity (radiance) for a large number of contiguous spectral bands. Every pixel in the image contains a continuous spectrum (in radiance or reflectance). This information can be used to characterize objects in the scene with great precision and detail. When using the term wavelength it is the center wavelength that it is referred to. [32]

The camera operating principle is illustrated in Fig. 11. The camera fore optic (focusing mirror) images the scene onto a slit which only passes light from a narrow line in the scene. After collimation, a dispersive element, a slit that separates the different wavelengths, and the light is then focused onto a detector array. The net effect of the optics is that each pixel interval along the line is defined by the slit. The corresponding spectrum is projected on a column of detectors on the array. The data read out from the array thus contains a slice of hyperspectral image, with spectral information in one direction and spatial (image) information in the other. [32]

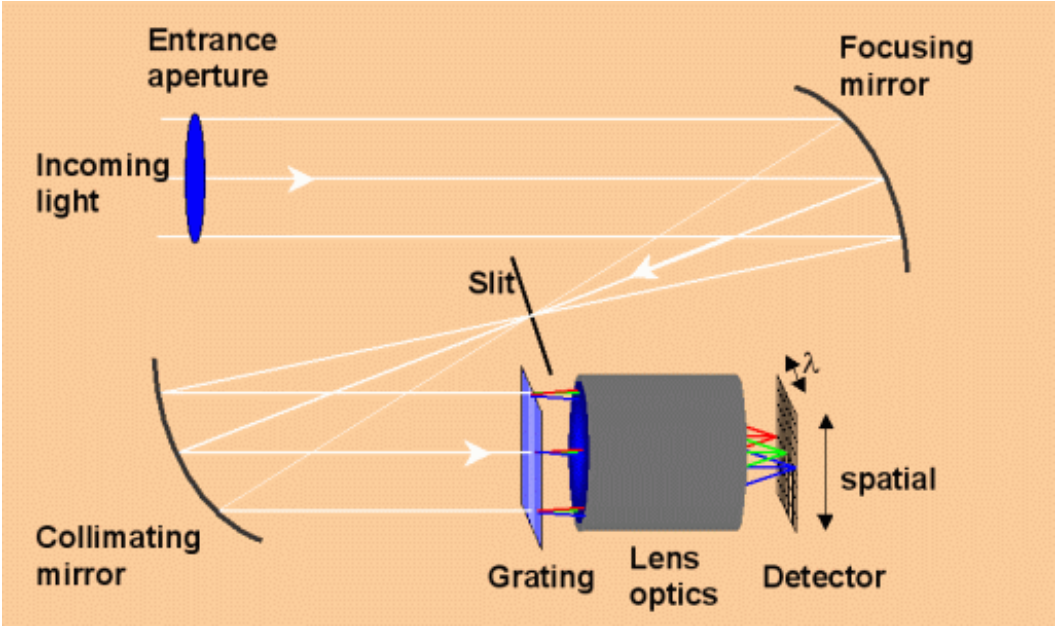

Figure 11: Principle drawing of how the hyperspectral camera operates. Incoming light hits the focusing mirror that guides the light through a slit and on to a collimating mirror. From the collimating mirror the light is led through a grating and into the lens. [32]

The scanning in this thesis is done by a linear translation of the scene, it means that the camera is static and the sample is placed on the translation stage. When scanning over the scene, the hyperspectral camera detects slices from adjacent lines to form a hyperspectral image or "cube" with two spatial dimensions and one spectral dimension. Every pixel in the image contains one full radiance spectrum. [32]

3.2.3 Rotation/translation stage

Stranda originally makes the manufactured translation stage and it has been modified by Norwegian Electro Optic for the use in this sort of experiments. The scanner table moves with help from a step motor[19]. It is difficult to say for certain how many steps the table moves, but since both the size of the wafer and the pixel resolution is known it possible so estimate the number of steps. The wafer is 50 mm in width and has about 156 pixels in the same direction. This information is employed to calculate that one step moves the translation stage approximately 32.0 μm. The computer governs the translation stage.

[19] Also called a stepper motor, this is a synchronous electric motor. The motor divides a full rotation into a large number of steps.

3.2.4 Cryogenic vessel

A cryogenic vessel is essentially an aluminum cylinder that is designed specially for this sort of cryogenic experiments. In this thesis a cryogenic vessel is used to freeze the multicrystalline silicon wafer. The cryogenic vessel is filled with liquid nitrogen for the freezing process. The liquid nitrogen is poured into the cryogen vessel until the temperature of the vessel reaches 123.5 K (-150°C) and then the cryogenic vessel is placed on the translation stage. When the temperature reaches 93 K (-180°C) the wafer is gently placed on the surface within the cryogenic vessel. 93 K was approximately the lowest reachable temperature when using this method. After a few seconds, the wafer is frozen and the measurements can start. The temperature rapidly increases so refill will be necessary to retain the low temperature. The freezing of the wafer changes the thermal properties in the semiconductor material.

3.2.5 Light sources

The light source used in this thesis to illuminate the wafer is a 2 W solid-state laser, a laser in which a semiconductor material produces the coherent output beam. The laser emits light with wavelength of 808 nm. This is in the infrared (IR) area, light that is visible for the human eye. The laser beam is very concentrated with an effect of 2 W, the concentration is approximately $4\times10^{18}\ photons/cm^3$. The concentration of one sun is $2\times10^{17}\ photons/cm^3$. The calculated laser intensity is approximately twenty suns. Since this is a strong laser with the intensity of 20 suns, protective goggles most be used at all time while the laser is operative to avoid damage to the eyes.

3.2.6 Filter

Second order refraction from the light source in the slit inside the camera can give unwanted effects when recording. IR-filters are used for filtering the light source. The filters have cut wavelength of 850 nm and 1000 nm. Normally, the 850 nm filter is used when illuminating with the laser and it is placed just below the camera lens. The filters are borrowed from the quasi-steady-state equipment.

3.2.7 Quasi-Steady-State Photoconductance (QSSPC) equipment

Since the knowledge of carrier lifetime is important in this thesis, the lifetime of the wafer is measured with the quasi-steady-state equipment. This equipment is delivered by Sinton Consulting Inc., and has the appellation "BCT-400 Photoconductance Tool". Read [33] for more information about the equipment. This equipment measures the carrier lifetime with the method described in the section 2.6.1.

The apparatus has to be directly in contact with the wafer and the light from the flash lamp is directed through a quartz rod. The flash lamp provides white light where its intensity reduces to zero over several milliseconds. The filter[20] with wavelength 850 nm is placed between the flash and the wafer to cut off some of the wavelengths from the flash. When light strikes the wafer it generates mobile carriers and it increases the conductivity in the sample. The coil measures the conductivity and the apparent carrier lifetime can be calculated. A reference cell placed inside the apparatus receives a fraction of the light that strikes the sample and measures the generation rate.

"This method for lifetime measurement is one of the most widely used techniques and it is important to understand the trapping effects and the impact it has on the photoconductance." [16]

3.3 Setup and execution

3.3.1 Quasi-steady-state photoconductance

The wafer is placed on a white table and the quasi-steady-state photoconductance apparatus is placed on top of the wafer. The apparatus is coupled to a computer, which illustrates how the lifetime varies across the wafer with different injection level Δn. It is important to place the coil in direct contact with the wafers surface or the results may become misleading.

3.3.2 Laser and hyperspectral camera

The hyperspectral camera detects the laser beam as a line across the wafer. This is why the wafer has to be placed on a scanner table and moved by using the translation stage.

[20] The filter is used to control the excess carrier profile

The camera is perpendicular to the wafer and laser strikes the wafer with an angle of 59°. The setup is illustrated in Fig. 12.

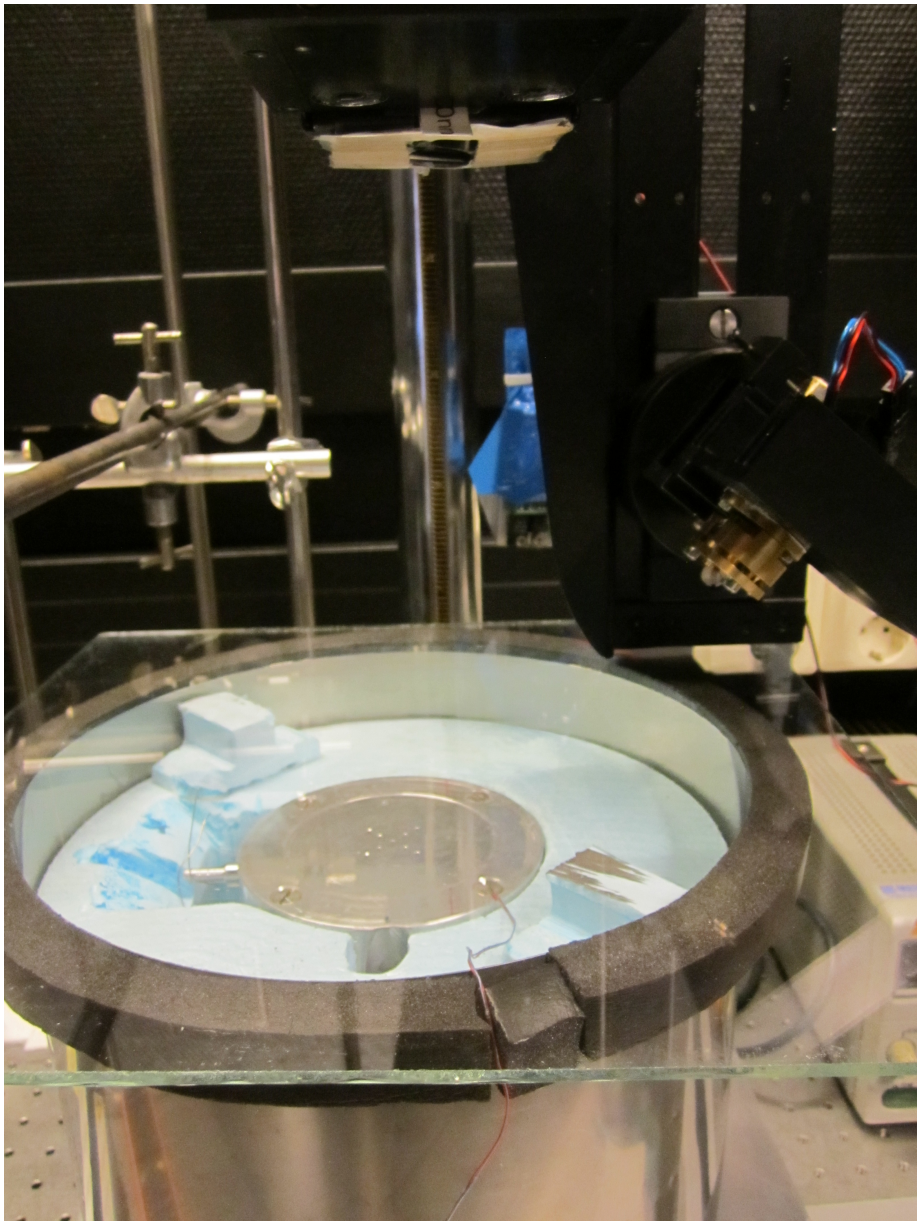

Figure 12: Experimental setup. The cryogenic vessel is placed on the translation stage and covered with a glass lid. The laser is located to the right and the hyperspectral camera at the top.

For calibration the laser and the camera is adjusted in both height and angle to make the measurements as accurate as possible. Since the laser and the camera is mounted together the distance between them are constant. The light is turned off during all measurements to avoid unwanted exposure from the surrounding elements in the lab. Aluminum surface of the scanning table is used since it reflects the photons back and gives them a new opportunity to interact with the atoms making up the wafer.

The technique for photoluminescence detection is the same for executing the measurements at 300 K and 93 K. The only difference is the sort of scanner table used.
At room temperature the wafer is placed on top of an adjustable table and the height is regulated until it is in the correct focus point. The wafer is then illuminated by the laser and recorded on the computer. The situation when the wafer is frozen is more complicated than at room temperature. The wafer is placed on the cryogenic vessel for the freezing process, which takes a few seconds. Then the laser illuminates the wafer in the same way as for room temperature. The glass lid on the cryogenic vessel comes in handy when measuring at low temperatures. The glass keeps warm air away from the constant flow of evaporated nitrogen that fills the area around the wafer, within the vessel. When the glass lid is removed, either for refill or for inserting the wafer, water vapor will occur in the open space between the aluminum surface and the glass lid. This will lead to frost on the aluminum and wafer surface. The frost will affect the intensity of the photoluminescence signal detected by the camera. During recording the glass lid needs to be removed due to reflection of the laser beam caused by the glass. This is because of the laser beams angle towards the surface of the glass and involves 50 % reflection, which will affect the results tremendously if not removed.

3.4 Data processing

This chapter deals with how the results from the recordings are handled and presented. There are several programs used to obtain the best results possible.

3.4.1 HYSPEX images

The “hyper” in hyperspectral means “over” as in “too many” and refers to the large number of measured wavelength bands. Hyperspectral images are spectrally over-determined, which means that they provide plentiful spectral information to identify and distinguish spectrally unique elements. [34]

The software used when recording is *“HYSPEX version 3.5”*, delivered by Norsk Electro Optikk AS. The recorded hyperspectral images are saved as HYSPEX files on the computer attached to the camera and the translation stage. The HYSPEX files contains metadata from every recording, all the information needed for further processing. In the *record options* the number of frames recorded is specified, decides how broad the

images will be. The high-signal-noise-ratio (HSNR) mode can be used for noise reduction in the image. Before new recordings can be performed the old background must be replaced. Covering the entrance of the camera with a black object and start background recording does this. *Scanning mode* decides the parameters of the translation stage such as "speed back". The *camera parameters* are the closing time, which is chosen to be between 50 μs and 200 μs in this experiment.

3.4.2 MATLAB

MATLAB is used for image processing and both functions and programs were built for this specific task. The commando *"read_HYSPEX_files_all"* opens the HYSPEX files in MATLAB. All 150 bands can be viewed as single images containing information for each of the 150 wavelengths recorded by the camera. The MATLAB commando *"view_HYSPEX_images_with_video"* views all 150 bonds as a movie. In this way it is possible see how the photoluminescence changes with increasing wavelength bands. In MATLAB the image filename was converted from HYSPEX to Tagged Image File format (TIF), so that they could be used in other image processing programs. Every MATLAB program and function used in this thesis is found in appendix A. The HYSPEX files analyzed in this thesis are listed in appendix B.

3.4.3 ImageJ

ImageJ is a public domain Java image processing and analysis program. ImageJ is used for image processing and illustration in this thesis. ImageJ can display multiple spatially related images in a single window. These image sets are called stacks[21]. The images that make up the stack are called slices. In MATLAB the HYSPEX file is converted to 150 TIF images, which is a format that ImageJ support. All 150 TIF images are loaded into ImageJ and converted to a stack. The stack, or parts of it, can be viewed as a montage[22]. The function *sum slices projection* creates a real image that is the sum of the chosen slices. Single pictures in TIF format may also be loaded into ImageJ for image processing. The filter *unsharpen mask* is an image manipulation technique. The "unsharp" of the name derives from the fact that the technique uses a blurred, or "unsharp", positive to create a "mask" of the original image. The unsharped mask is then combined with the negative, creating the illusion that that the resulting image is sharper than the original. *Enhance*

[21] In a stack, a pixel becomes a voxel (volumetric pixel), i.e., an intensity value on a regular grid in 3D space.
[22] A single pictorial composition made by juxtaposing many pictures.

contrast enhances the contrast in an image using histogram equalization. Both these techniques may enhance noise in the image and are image manipulation techniques. This is why they are always illustrated with their original images to see the changes done to the image.

3.4.4 Multivariate image analysis

Multivariate statistical analysis is used in order to understand the relationship among the variables and to find relationships to external physical and other related features in these multivariate images.

The hyperspectral image file is loaded into MATLAB workspace and opened with the program multivariate image analysis (miagui) where the image is cropped in such way that unnecessary information (background) in the image is removed. The cropped image is then saved as a dataset. The principal component analysis can only be performed on a matrix ($IJ \times k$). The program *PLS_Toolbox* for principal component analysis is opened by typing *browse* in the command window in MATLAB. When building the model the recommended number of principal components is chosen such that most of the structure information in the original dataset is modeled. This is found by analyzing the plot of cumulative covariance captured in percent for each principal component. The unstructured information such as noise is saved in the residual matrix E. It is possible to choose more than the recommended number of principal components to extract more information. Thus, the principal components will be of little interest for information extraction. Each principal component extracts a particular spectral feature (a linear combination of the intensities over all the wavelengths) from the image. The reorganized score matrix is a representation of the image in terms of that spectral feature. The loading matrix contains information about the variables (wavelengths).

Table 2: Band with their corresponding energy (eV) and center wavelength (nm).

Band	λ (nm)	E (eV)	Band	λ (nm)	E (eV)	Band	λ (nm)	E (eV)
1	937	1.324	51	1192	1.041	101	1446	0.858
2	943	1.316	52	1197	1.037	102	1451	0.855
3	948	1.309	53	1202	1.032	103	1456	0.852
4	953	1.302	54	1207	1.028	104	1462	0.849
5	958	1.295	55	1212	1.024	105	1467	0.849
6	963	1.288	56	1217	1.019	106	1472	0.843
7	968	1.282	57	1222	1.015	107	1477	0.840
8	973	1.275	58	1227	1.011	108	1482	0.837
9	978	1.269	59	1233	1.006	109	1487	0.834
10	983	1.262	60	1238	1.002	110	1492	0.832
11	988	1.256	61	1243	0.998	111	1497	0.829
12	993	1.249	62	1248	0.994	112	1502	0.826
13	999	1.242	63	1252	0.990	113	1507	0.823
14	1004	1.236	64	1258	0.986	114	1512	0.821
15	1009	1.230	65	1263	0.982	115	1518	0.817
16	1014	1.224	66	1268	0.978	116	1523	0.815
17	1019	1.218	67	1273	0.975	117	1528	0.812
18	1024	1.212	68	1278	0.971	118	1533	0.809
19	1029	1.206	69	1283	0.967	119	1538	0.807
20	1034	1.200	70	1289	0.963	120	1543	0.804
21	1039	1.194	71	1294	0.959	121	1548	0.801
22	1044	1.188	72	1299	0.955	122	1553	0.799
23	1049	1.183	73	1304	0.951	123	1558	0.796
24	1054	1.177	74	1309	0.948	124	1563	0.794
25	1060	1.170	75	1314	0.944	125	1568	0.791
26	1065	1.165	76	1319	0.941	126	1574	0.788
27	1070	1.160	77	1324	0.937	127	1579	0.786
28	1075	1.154	78	1329	0.934	128	1584	0.783
29	1080	1.149	79	1334	0.930	129	1589	0.781
30	1085	1.144	80	1339	0.927	130	1594	0.778
31	1090	1.138	81	1345	0.922	131	1599	0.776
32	1095	1.133	82	1350	0.919	132	1604	0.774
33	1100	1.128	83	1355	0.916	133	1609	0.771
34	1105	1.123	84	1360	0.912	134	1614	0.769
35	1110	1.118	85	1365	0.909	135	1619	0.766
36	1116	1.112	86	1370	0.906	136	1624	0.764
37	1121	1.107	87	1375	0.902	137	1629	0.762
38	1126	1.102	88	1380	0.899	138	1635	0.759
39	1131	1.097	89	1385	0.896	139	1640	0.757
40	1136	1.092	90	1390	0.893	140	1645	0.754
41	1141	1.087	91	1395	0.889	141	1650	0.752
42	1146	1.083	92	1401	0.886	142	1655	0,75
43	1151	1.078	93	1406	0.882	143	1660	0.747
44	1156	1.073	94	1411	0.879	144	1665	0.745
45	1161	1.069	95	1416	0.876	145	1670	0.743
46	1166	1.064	96	1421	0.873	146	1675	0.741
47	1172	1.059	97	1426	0.870	147	1680	0.739
48	1177	1.054	98	1431	0.867	148	1685	0.736
49	1182	1.050	99	1436	0.864	149	1691	0.734
50	1187	1.045	100	1441	0.861	150	1696	0.732

4. Results and discussion

In this study there were executed approximately 100 hyperspectral measurements. The results from the measurements are illustrated and discussed in this chapter.

4.1 Quasi-steady-state photoconductance measurements

The quasi-steady-state photoconductance technique was employed to measure the lifetime of minority carriers in the multicrystalline silicon wafer. The areas of the wafers that were examined are illustrated in Fig. 13.

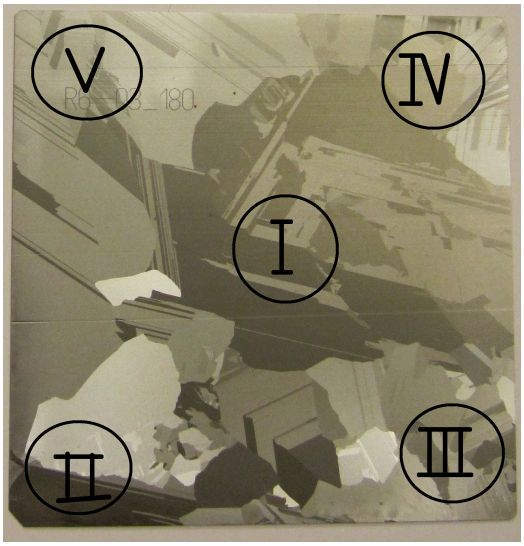

Figure 13 Areas of the multicrystalline wafer that were investigated with the QSSPC technique.

The purpose of these measurements is to get an overview of how long the minority carriers will reside in the conduction band before recombining through one of the recombination routes. As shown in Table 3, the measured carrier lifetime varies across the wafer.

Table 3: Measured lifetime at specific areas of the wafer

Area on the wafer	Measured Lifetime
Area I	54.3 μs
Area II	39.5 μs
Area III	35.1 μs
Area IV	49.3 μs
Area V	25.6 μs

The result from the quasi-steady-state photoconductance measurements at Area I is illustrated in Fig. 14, which shows the minority carrier lifetime as a function of minority carrier density.

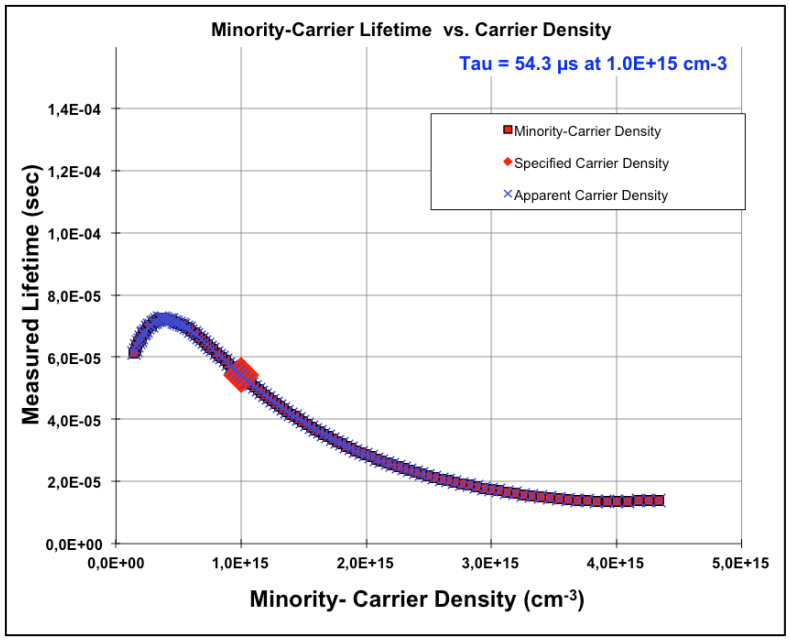

Figure 14: Result from the measured lifetime vs. carrier density at Area I.

The wafer examined in this thesis is doped with boron and contains a large quantity of defects as mentioned in section 3.2.1. A considerable consequence of these defects is that the results from the quasi-steady-state photoconductance measurements for carrier lifetime will be drastically affected. These defects cause significant problems in photoconductance measurements since they induce an abnormal effect that masks the actual recombination lifetime.

In multicrystalline silicon the recombination mechanisms usually coexist and carrier-trapping effects generally hinders them. The analysis of the injection dependence of the minority carrier lifetime provides an insight into the trapping effect on the recombination lifetime. Cuevas et al. explained that trapping results in an abnormally high apparent lifetime under low illuminations conditions, and under increasing injection level the apparent lifetime decreases drastically. In Fig. 14 this effect of abnormal high apparent lifetime is illustrated. At low injection level the measured lifetime increases while at higher injection levels the measured lifetime decreases. It is assumed impossible to get correct results from the quasi-steady-state photoconductance measurements in this multicrystalline silicon wafer at low injection levels due to the prominent trapping effect.

Daniel H. Macdonald explains that when trapping is present the calculated apparent lifetime is incorrect for two reasons: 1) The assumption of equal free electron and hole densities breaks down, $\Delta n \neq \Delta p$. 2) A large number of extra holes are present. Eq. (2.35) is used for calculating the apparent lifetime and is given by: $\tau_{app} = \Delta\sigma / G_e(\mu_n + \mu_p)$. Since this is a boron-doped multicrystalline silicon wafer the majority carriers are holes. Cuevas et al explained that for a given steady-state photo-generation rate, G_e, in boron-doped silicon wafer, an excess minority carrier concentration is created so that recombination is perfectly balanced by: $\Delta n = G_e \tau_r$. At the same time an additional number of electrons, n_t, is trapped. To maintain charge neutrality, the concentration of excess majority holes needs to be $\Delta p = \Delta n + n_t$. Since electrons are trapped they are not mobile, while holes are mobile and they will additionally increase the photoconductance as described by the Eq. (2.35). The increase in measured photoconductance result in a high apparent lifetime. From these results, the fact that the measured apparent lifetime is abnormal high there exist a large density of traps in this multicrystalline silicon wafer.

4.2 Photoluminescence imaging

Photoluminescence of silicon is an effect of the radiative band-to-band recombination mechanism. The radiative recombination process emits photons with approximately the given energy of the forbidden band gap. The hyperspectral camera used in this thesis detects photoluminescence in the wavelength range 937 nm - 1696 nm. The radiative band-to-band recombination is competing with recombination through energy levels within the forbidden band gap introduced by defects. Because the properties of the silicon semiconductor are temperature dependent, the wafer was examined at temperatures of 300 K and 93 K. This section only investigate photoluminescence of silicon, while section 4.3 investigate inter band gap photoluminescence.

4.2.1 Photoluminescence imaging at 300 K

The wafer was examined at 300 K and the recorded bands are shown in Fig. 15, the montage made in ImageJ. The montage is used to illustrate all 150 bands in the same image making it possible to detect the appearance of photoluminescence at all wavelengths recorded by the hyperspectral camera.

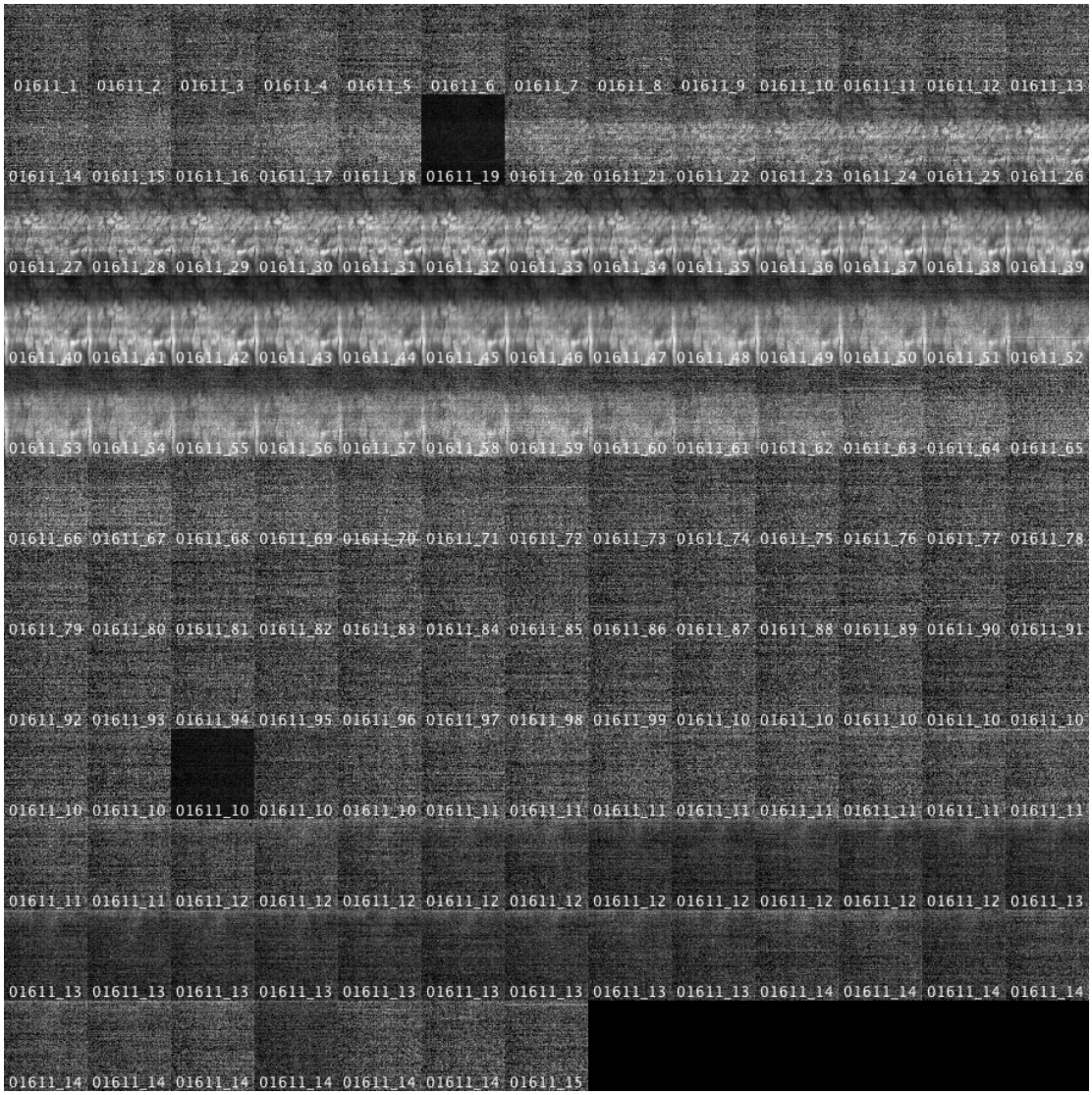

Figure 15: Montage of the recorded bands at 300 K. The Photoluminescence detected by the hyperspectral camera, the wavelengths increase with increasing band number.

The montage in Fig. 15 reveals that the first detected photoluminescence signal appears in band 23 and the signal becomes more evident with increasing band number. The most evident photoluminescence images of silicon are found from band 27 to band 40, which has the corresponding energy range 1.160 eV – 1.092 eV. After band 40 the photoluminescence image gradually vanishes, the contrast in the image becomes less evident. Band 19 and band 107 appear black in the montage. They are caused by "bad pixels" detected by the camera. To achieve the best photoluminescence image of silicon as possible all the bands that have the most evident signal are added together. Fig. 16 is the sum of all bands from 30 to 40. Fig. 17 is the result of the unsharpen mask used on the image in Fig. 16. The unsharpen mask is applied on image to enhance the spectral characteristic feature in the image.

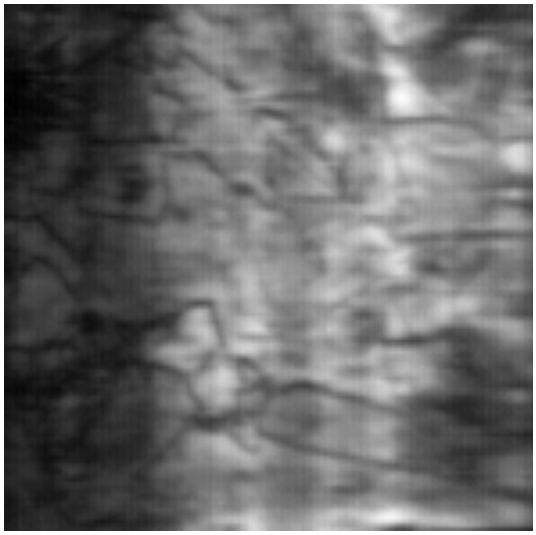

Figure 16: The photoluminescence image of silicon. Bands from 30 to 40 added together.

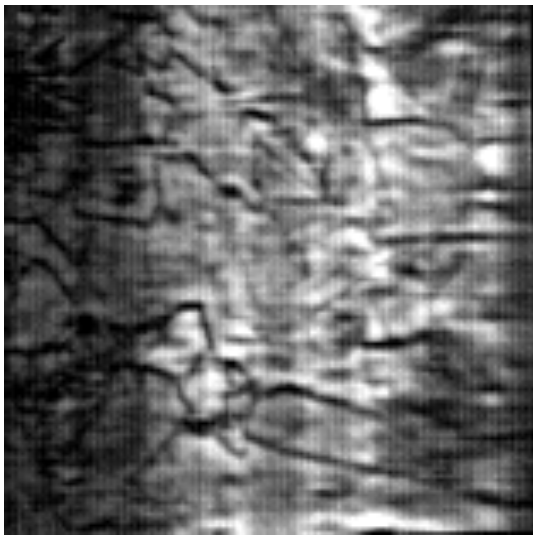

Figure 17: Result of the unsharpen filter used on the photoluminescence image of silicon.

The brightest areas in Fig. 16 are where the detected photoluminescence has its strongest signal, while the darker areas are where the photoluminescence signal is lower. In the black areas the photoluminescence signal is assumed zero. The dark part to the left in Fig. 16 that looks like a straight line across the image is an effect of the unstable intensity of the laser beam. This effect makes it difficult to extract information about the structure in the wafer at the distorted area. The characteristic features in Fig. 16 is enhanced by using unsharpen filter on the image and the result is displayed in Fig. 17. The location and size of the dark patterns are more evident in Fig. 17, but the filter also increases noise in the image. The dark line patterns in the image are known as grain boundaries. Some of the grain boundaries are more evident than others. At 300 K the dark lines are broad and the location is evident. Disregarding the unstable laser effect, the dark lines are grain boundaries while the brighter areas are the detected photoluminescence of silicon. Fig. 16 is referred to as the photoluminescence image of silicon at 300 K.

For a closer look at the location of the grain boundaries in the wafer, the most evident of the grain boundaries are recreated in an image of the original wafer. The image of the wafer is taken with a compact camera, when the wafer had the “wrong side up”. The “wrong side” is the side of the wafer turned down while illuminating. The reason for this is because the signal detected by the camera is inverted when saved on the computer.

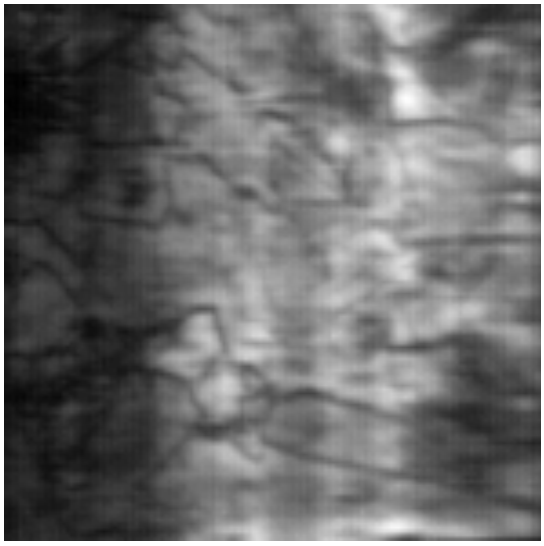

Figure 18: The photoluminescence image of silicon.

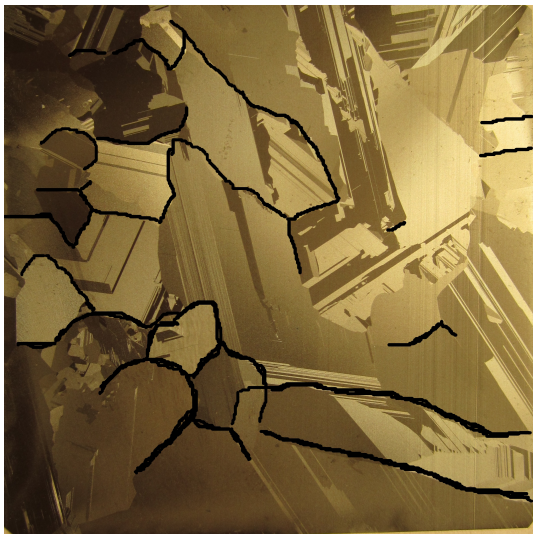

Figure 19: Image of the wafer in which the grain boundaries are recreated.

Some of the characteristic structures in the photoluminescence image, Fig. 18, are easily detected and recreated in in Fig. 19. The grain boundaries are located at the edges of the large crystals. The straight lines in Fig. 18 are known as twin-boundaries. These twin boundaries are not visible in the photoluminescence image recorded at 300 K.

The spectral information from the recorded data at 300 K was collected and the photoluminescence spectrum is illustrated in Fig. 19. The collected data is from an area in the wafer where the strongest photoluminescence signal from silicon was detected.

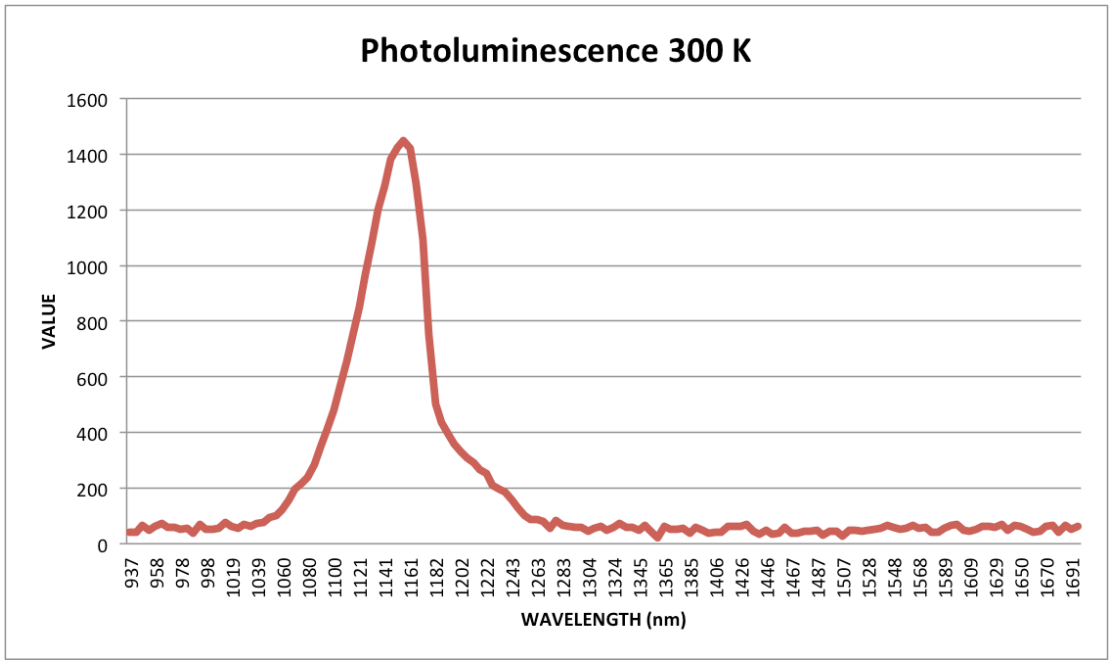

Figure 20: Photoluminescence spectra of silicon detected at 300 K. The photoluminescence signal has its peak value at 1151 nm. The peak occurs in the wavelength range 1060 nm – 1243 nm.

At 300 K the photoluminescence spectrum of silicon is displayed in Fig. 20. The vertical axis, with the term "VALUE", is the detected intensity of the photoluminescence signal. The horizontal axis is all wavelengths detected by the hyperspectral camera. Fig. 20 reveals that the signal has its peak value at wavelength 1151 nm, and according to Table 2, this corresponds to 1.078 eV and occur in band 43. The spectrum of silicon was expected to occur from band 24 to band 61, discovered in the montage. From Fig. 19 the spectrum of silicon occurs in the wavelength range 1060 nm – 1243 nm and this is from band 25 to band 61. The signal detected at other wavelengths is approximately at value 50, which is about 29 times less than the peak value of the silicon spectrum. This indicates that there is little noise in the recorded bands at 300 K. The asymmetrical shape at the end of the spectra resembles a shoulder. The shoulder is an effect of multi-phonon interaction, which is explained by the recombination of carriers through the band gap with the assistance phonons [26]. The quantity of carrier-phonon-interactions increases with increasing temperature. The silicon spectrum detected at 300 K is relatively broad.

The size of the band gap of silicon changes with different temperature as mentioned in section 2.2.2 At 0 K the band gap is 1.17 eV as Fig. 2 indicates. At 300 K the size of the band gap is 1.1245 eV derived from Eq. (2.4). This energy level is found between band 33 and 34. The given wavelength for this energy level is found by interpolating between the two bands. From the interpolation, the corresponding wavelength of the energy level 1.1245 eV is 1103.5 nm. At 300 K the semiconductor is, from Fig. 5, in the saturation range with the ionization degree $f_A = 1$ found in Fig. 6. This means that all acceptor atoms are assumed completely ionized $N_A^- \approx N_A$. This is due to the shift in Fermi level towards the middle of the band gap with increasing temperature [26]. In this case every acceptor atom has given up their extra hole and the density of holes in the valence band increases. When the temperature increases the density of thermal excited excess carriers increases, which results in increasing density of electrons in the conduction band and holes in valence band. The increasing carrier densities in both bands result in a diminishing band gap size. The radiative band-to band recombination is affected by the temperature dependency of the band gap. Thus, the photoluminescence spectrum is temperature dependent. Since silicon is an indirect-band-gap semiconductor it is in general a poor emitter of light. The main reason for this, according to [27], is that the fast non-radiative recombination route dominates the slower radiative recombination route at 300 K. They are competing since the radiative band-to-band recombination mechanism and the non-radiative recombination

mechanism occur simultaneously in the silicon semiconductor. The non-radiative recombination mechanism is the Shockley-Read-Hall recombination, recombination through energy levels within the forbidden band gap. These levels are introduced by defects in the crystal. As mentioned in section 2.4.1, the Shockley-Read-Hall recombination is also called "multi phonon" recombination. At this excess carrier concentration, approximately 10^{15} cm^{-3}, multi-phonon recombination dominates both Auger and radiative recombination at shown in Fig. 8. At room temperature there is a large density of phonons available for electron interaction. As mentioned in section 2.3.3 there are two main electron scattering mechanisms, and those are phonon and impurity scattering. Even though phonon interaction is the dominant mechanisms at 300 K the carrier mobility is also affected by impurity scattering. This is because all impurity atoms are assumed ionized and they scatter electrons more efficient than non-ionized impurities. When electrons move in the conduction band before recombining their mobility will be affected by phonon-interactions and impurity scattering. It is believed that the multi-phonon interaction mechanism causes the non-radiative effect at high temperatures. Also, at 300 K the temperature is too high to activate carriers out of traps, which limits the probability of recombining through them.

As mentioned in section 2.1.2 impurities segregate along grain boundaries because they are more electrically reactive than the grains themselves. The hyperspectral camera only detected photoluminescence from silicon and not from defects at 300 K. Since non-radiative recombination is recombination without emitting photons and this is the dominant process, recombination through defect is not detectable by the camera. The grain boundaries found in the photoluminescence image of silicon in Fig. 16 are relatively broad, which is due to the mobility of minority carriers in the semiconductor. At 300 K the mobility of carriers are limited by both phonon interaction and ionized impurity scattering. Because of the phonon-interaction with excess carriers there is only a small quantity of the minority carriers that will diffuse from the "good" areas in the wafer to the grain boundaries to recombine there. Those that reach the boundaries recombine non-radiatively. They recombine at the grain boundaries since that is where impurities segregate, and they as well as the grains are viewed dark in the photoluminescence image 16. This could explain why the grain boundaries detected are broad. And why photoluminescence from grains is not detectable at 300 K.

4.2.2 Photoluminescence imaging at 93 K

The wafer was examined at 93 K to investigate the photoluminescence at low temperatures. The results from the recording are viewed in a montage made in ImageJ. Fig. 20 is the montage of the recorded 150 bands at 93 K. The montage makes it possible to detect in which bands photoluminescence occur.

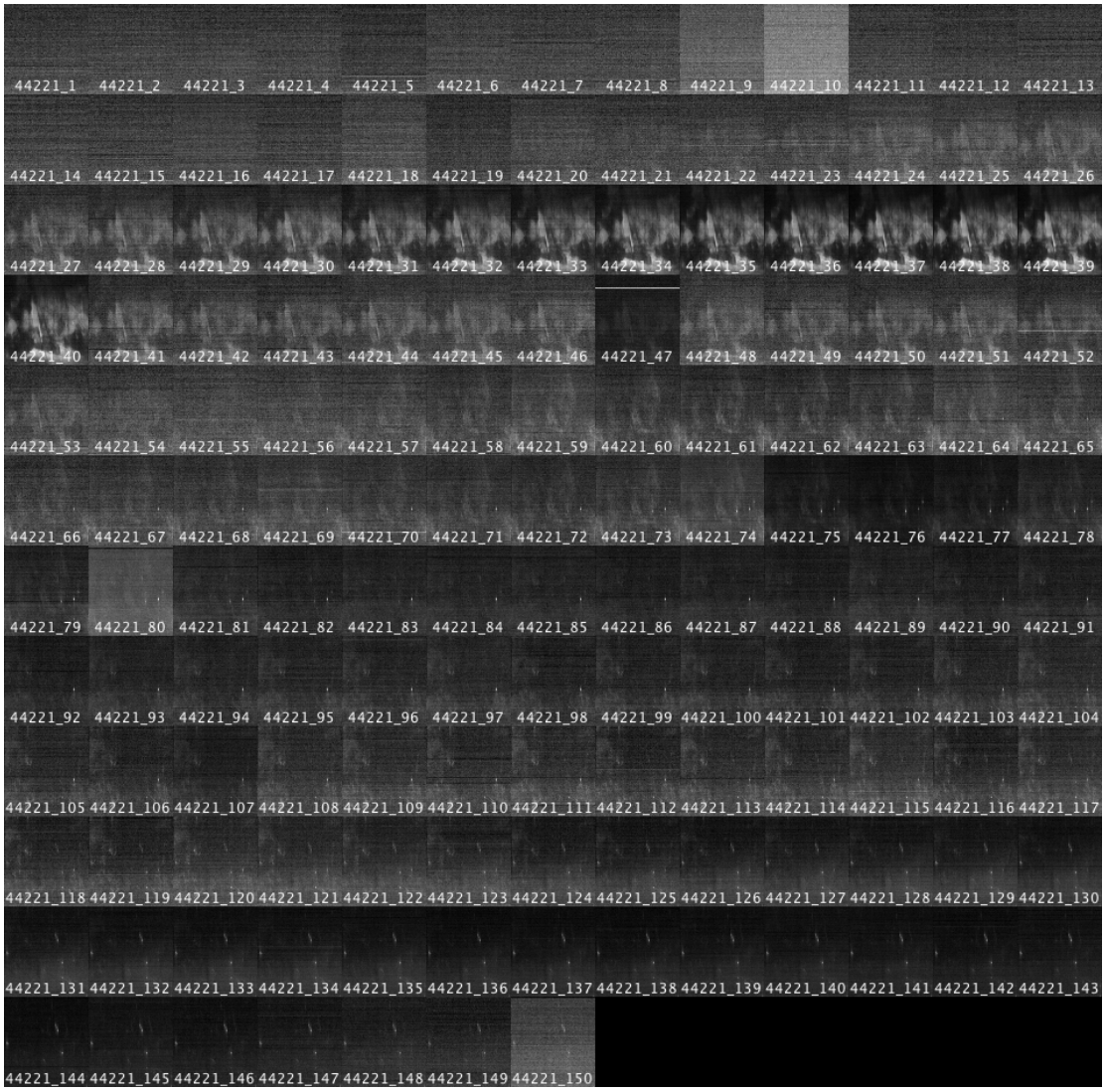

Figure 21: Montage of the recorded bands at 93 K. Photoluminescence detected by the hyperspectral camera, the wavelengths increase with increasing band number.

From Fig. 21, the montage, it is evident in which bands the photoluminescence of silicon occurs. At roughly band 24 the photoluminescence signal becomes detectable, the signal increases with increasing wavelength, i.e. band number. From band 30 to band 39 the photoluminescence of silicon has the strongest detected signal, which is in the energy range 1.144 eV - 1.097 eV. After band 39 the photoluminescence signal gradually vanishes until band 53. Contrary to the montage of the recording at 300 K, this montage reveals photoluminescence from defects. Inter band gap photoluminescence is detected

in a lower energy range than the detected photoluminescence of silicon. Inter band gap photoluminescence detected in this montage are illustrated and discussed in section 4.3.

The most evident photoluminescence images of silicon occurs in the wavelength range 1085 nm - 1131 nm, as shown Fig. 21. To achieve the best photoluminescence image of silicon as possible all bands with the most evident signal are added together. In Fig. 22 all bands from 30 to 39 added together. Fig. 23 is the result of unsharpen mask used on the image in Fig. 22 to enhance spectral features.

Figure 22: Photoluminescence image of silicon at 93 K. All bands from 30 to 39 added together.

Figure 23: Unsharpen filter used on the photo-luminescence image in Fig. 22.

Fig. 22 reveals different features in the wafer than Fig. 16. Especially, the grain boundaries are not as broad and clear, and there seems to be small grain structures, sub-grains, within the bright areas of the image. The structure is more evident in Fig. 22 than in Fig. 16. In Fig. 23 the features in the image is clearer, but it is important to have in mind that the filter also enhances noise. In Fig. 22 the variations in the laser beam intensity cause the same effect as in Fig. 16. As opposed to the photoluminescence image in Fig. 16, the dark area occurs in the top of these images. There is impossible to extract any information about the structure in these dark areas. At 93 K the twin-boundaries are detectable in the photoluminescence image where they are visible as straight bright lines. If the laser beam variation is disregarded, the bright areas are associated with photoluminescence of silicon while the dark areas are where no signal detected. The most evident grain boundaries detected in the photoluminescence image of silicon is recreated in an image of the wafer. Fig. 24 is the photoluminescence image of silicon at 93 K and Fig. 25 is the image of the multicrystalline wafer examined.

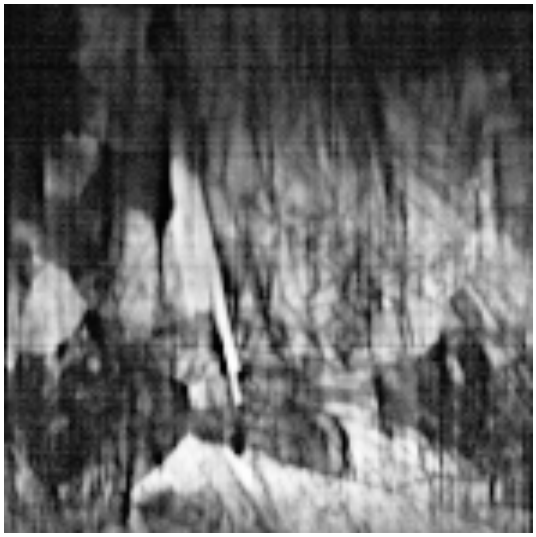

Figure 24: Photoluminescence image of silicon at 93 K.

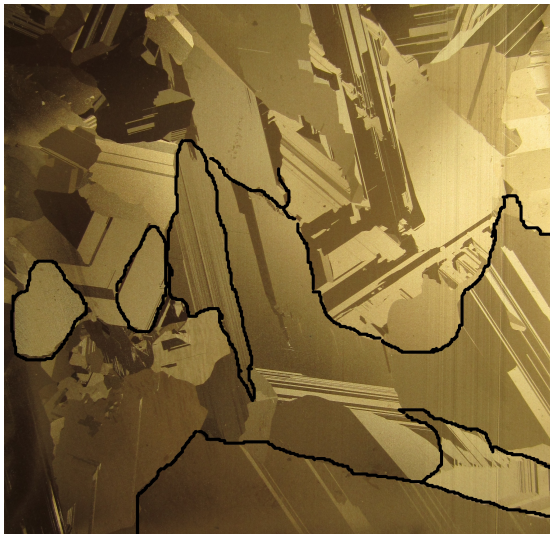

Figure 25: Image of the wafer in which the grain boundaries are recreated.

Some of the large crystals in the wafer are easily detected in the photoluminescence image of silicon in Fig. 24 and recreated in Fig. 25. The grain boundaries detected at 93 K are more difficult to recreate than they were at 300 K. The straight bright lines found in Fig. 24 are twin-boundaries.

Fig. 26 shows the photoluminescence spectra at 93 K. The data was collected from an area in the wafer where the strongest photoluminescence signal of silicon was detected.

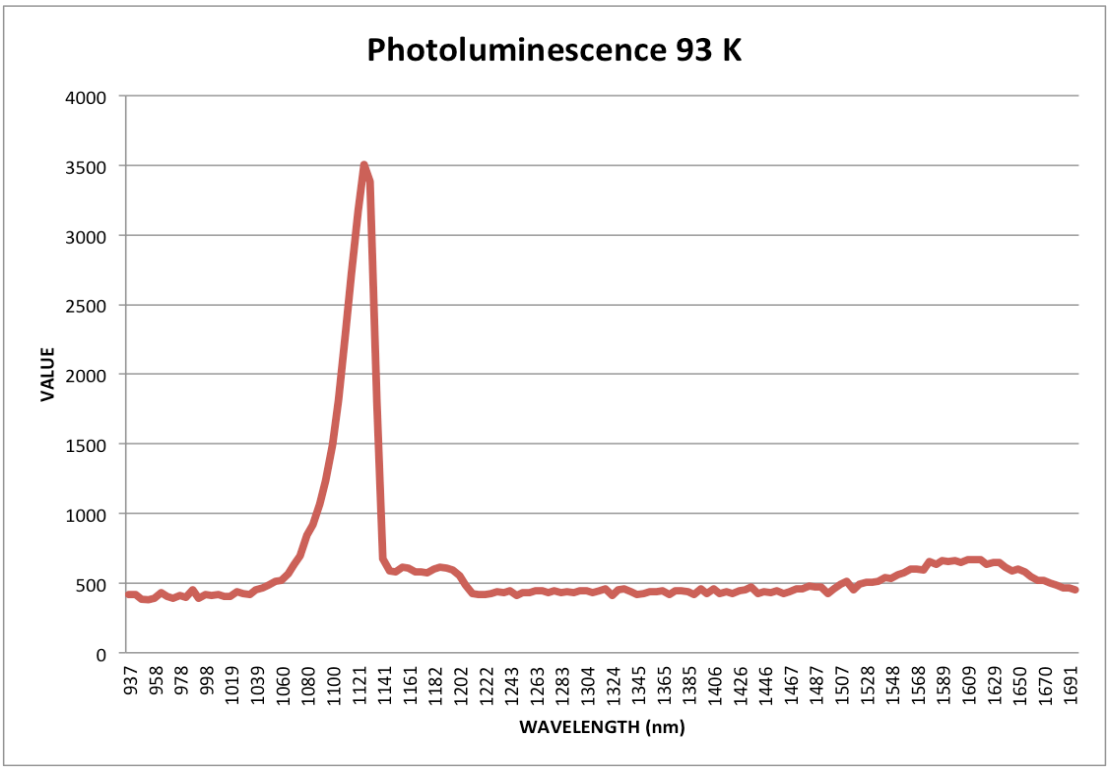

Figure 26: Photoluminescence spectra detected at 93 K. The photoluminescence of silicon occur in the wavelength range 1060 nm – 1202 nm. Its peak value is found at 1121 nm.

The photoluminescence spectrum of silicon is illustrated in Fig. 26. The vertical axis, with the term "VALUE", is the detected intensity of the photoluminescence signal. The horizontal axis is all wavelengths detected by the hyperspectral camera. At wavelength 1121 nm the signal has its peak value, and according to table 2 this has the corresponding energy of 1.107 eV and occur in band 37. The photoluminescence spectrum of silicon was expected, from the montage, to occur from band 24 to band 52. Fig. 26 shows that the photoluminescence signal from silicon occurs in the wavelength range 1060 nm – 1202 nm, which is found from band 25 to band 55. The signal detected at other wavelengths is approximately at value 490, which is about 7 times less than the peak value photoluminescence signal. This is a higher noise value than detected at 300 K. The shoulder-like feature at the end of the photoluminescence spectrum of silicon found in Fig. 26 is smaller though more defined than the one found in Fig. 20.

The photoluminescence spectrum of silicon at 93 K differs from the one at 300 K. In Fig. 27 these two photoluminescence spectra are plotted together to illustrate the difference. The photoluminescence spectrum at 93 is red and the spectrum at 300 K is green.

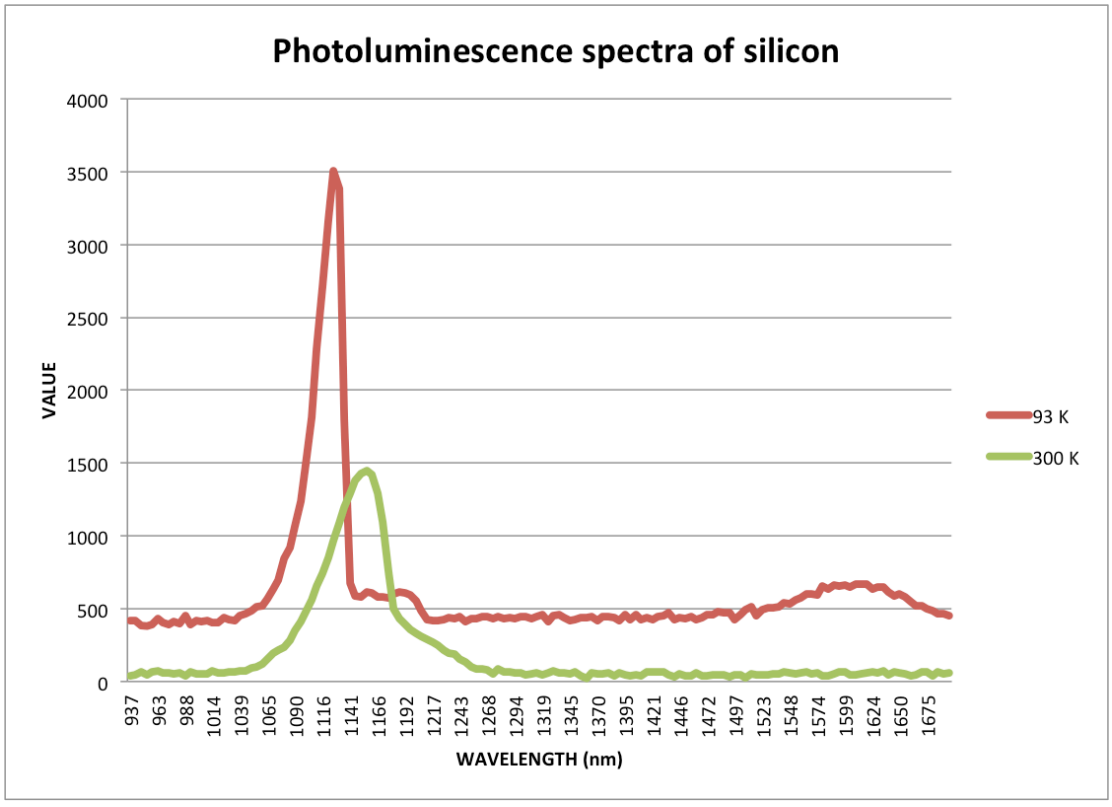

Figure 27: Photoluminescence spectrum of silicon at 300 K and 93 K plotted together. The peak value for 93 K are higher than for 300 while the signal is spectrally broader for 300 K.

Fig. 27 illustrates the different photoluminescence spectra detected at the two temperatures. The intensity of the signal is higher at 93 K than at 300 K. Thus, this is not a considerable difference. The photoluminescence spectrum at 93 K is spectrally narrower than at 300 K and the shoulder is smaller.

The assumption made for a boron-doped semiconductor is invalid for temperatures much lower than 300 K. From Fig. 5 it is shown that the semiconductor is in the "freeze-out" range at 93 K. When the temperature decreases the number of ionized atoms decreases. At 93 K the ionization factor, found in Fig. 6, equals 0.6. This means that 40 % of the acceptor atoms will not give up their extra hole to the valence band. This effect is caused by a shift in the Fermi level towards the valence band when the temperature decreases. This causes the density of holes in the valence band to decrease. The concentration of thermal excited carriers to the conduction band is assumed to be zero at sufficient low temperatures. These effects cause the band gap size to increases with decreasing temperature. The energy band gap size at 93 K is derived from Eq. (2.4) and is approximately 1.1644 eV. This energy level is found between band 26 and band 27. The corresponding wavelength is found by interpolating between the energy levels found in these two bands. The wavelength that corresponds to this energy level of 1.1644 eV is calculated to be 1065.3 nm. The photoluminescence of silicon occurs in the two montages at the same wavelength, this is also illustrated in Fig. 27. The photoluminescence peak at 93 K occurs at a shorter wavelength, higher energy, than the peak at 300 K. Thus, the spectrum is broader at 300 K than at 93 K. This is because the photoluminescence spectrum, as mentioned earlier, is temperature dependent. The overall photoluminescence intensity seems to increases some upon decreasing temperature.

Since the wafer examined is an indirect semiconductor the relaxation of an electron from the conduction band to the valence band has to involve phonon interactions for momentum conservation. The narrowing of the spectra and the reduction in shoulder size at 93 K is due to less phonon interactions. The probability of multiple phonon interaction with electrons relaxing from the conduction band to the valence band is strongly temperature dependent. The small shoulder at 93 K lasts from band 41 to band 49, which is in the wavelength range 1141 nm – 1183 nm. The montage, Fig. 21, reveals that the evident photoluminescence image of silicon is constant throughout this wavelength range. This explains why the shoulder has a constant height through this wavelength range. As for the recorded photoluminescence image of silicon at 300 K, the

image gradually vanishes in the wavelength range 1182 nm – 1250 nm. The shoulder becomes detectable at the same wavelength of 1182 nm in both peaks. The temperature dependence of phonon-interaction causes these two different shoulders to occur.

As mentioned, the characteristic features in Fig. 22 differ from the detected features in Fig. 16. The grain boundaries found in the photoluminescence image of silicon recorded at 300 K were broader than the one found in the image recorded at 93 K. The narrowing of the detected grain boundaries is explained by the carrier mobility in the material. The decreasing lattice vibration due to decreasing temperature implies that the possibility of phonon-electron interaction decreases. The impurity scattering of electrons is alo believed to be a limiting factor for electron mobility at low temperatures. But since the density of ionized impurities are reduced by 40 %, and they are the most effective scattering mechanisms, the over all impact of impurity scattering is less at lower temperatures. At low temperatures carriers move slower and longer before recombining, which increases the possibility for minority carriers to recombine at grain boundaries. A larger quantity of electrons diffuses to the grains from the "good" areas in the wafer, which contributes to the narrowing of the grain boundaries. At low temperatures states within the band gap become radiatively active, this means that the non-radiative recombination is not the dominant recombination route anymore. Thus, recombination through traps is still the dominant process due to the same injection level. The term "multi-phonon" is an incorrect name for Shockley-Read-Hall recombination at low temperatures, because minority carriers that recombine through intermediate levels at low temperatures emit photons. Also, at 93 k the temperature is low enough to discourage thermal activation of carriers out of traps. This increases the probability for recombination through traps. The detected dark line patters in the photoluminescence image in Fig. 22 are most likely to be grains, not grains and grain boundaries. This is due to the increased density of available electrons for recombination at these sites at low temperatures.

4.3 Defect photoluminescence imaging

Due to a large quantity of defect in the multicrystalline silicon wafer the appearance of photoluminescence from other elements than silicon is expected. The quasi-steady-state photoconductance measurements supported the assumptions of high defect density in the wafer examined in this thesis. Defect photoluminescence refers to inter band gap

photoluminescence detected from defects. The multicrystalline wafer was examined at 300 K and 93 K for defect photoluminescence imaging.

4.3.1 Defect photoluminescence detection at 300 K

At room temperature the detected photoluminescence was solely from silicon. In the montage, Fig. 15, defect photoluminescence were not detected in any bands. At room temperature the dominant process is the non-radiative recombination through energy levels within the band gap. Non-radiative recombination is a result of the phonon-interaction with excess carriers and ionized impurity scattering of excess carriers. One other factor is that at 300 K the temperature is to high to discourage thermal activation of carriers out of the traps. This decreases the probability for minority carrier recombination through traps. Since there are no detectable photoluminescence signals from defects, all recombination through states in the band gap introduced by defects are non-radiative.

4.3.2 Defect photoluminescence detection at 93 K

Defect photoluminescence were detected from the recording at 93 K. In the montage, Fig. 21, photoluminescence from defects than were found in a lower energy range than the occurrence of photoluminescence of silicon. In this section the detected photoluminescence from defects are illustrated by using the software ImageJ. Defect such as impurities incorporated in the silicon crystal gives rise to energy levels within the forbidden band gap. Some elements introduce multiple energy levels. Table 4 displays the different energy levels that the elements introduce in the band gap. All information found in Table 4 is calculated from the information about the energy levels found in Fig. 9 [11] and information found in [8]. The energy levels introduced by the iron-boron pair were found in [19]. Since the band gap increases with decreasing temperature the band gap energy for each temperature is derived from Eq. (2.4) and the energy levels are estimated from the value derived for each band gap size at 300 K and 93 K. Table 4 does not include every element found in [11, 8]. The energy levels introduced by elements that are within the energy range of photoluminescence of silicon and those with energy levels not detectable by the camera are excluded from Table 4.

Table 4: Energy levels within the band gap introduced by different elements.

Element	300K (Eg=1.1245 eV)		93K (Eg=1.1644 eV)	
	From Ev (eV)	*From Ec (eV)*	*From Ev (eV)*	*From Ec (eV)*
Fe	0.985	0.140	1.024	0.140
Fe	0.855	0.270	0.894	0.270
Fe	0.400	0.725	0.400	0.764
O	0.965	0.160	1.004	0.160
O	0.745	0.380	0.784	0.380
O	0.410	0.715	0.410	0.754
Cu	0.400	0.725	0.400	0.764
Cu	0.240	0.885	0.240	0.924
Ni	0.715	0.410	0.754	0.410
Ni	0.220	0.905	0.220	0.944
Ni	0.775	0.350	0.814	0.350
Co	0.350	0.775	0.350	0.814
Al	0.430	0.695	0.430	0.734
Cr	0.950	0.220	0.944	0.220
Cr	0.310	0.815	0.310	0.854
Cr	0.220	0.905	0.220	0.944
Cr	0.715	0.410	0.754	0.410
Mn	0.250	0.875	0.250	0.914
Mn	0.705	0.420	0.744	0.420
Ti	0.300	0.825	0.300	0.864
Ti	0.865	0.260	0.904	0.260
V	0.300	0.825	0.300	0.864
V	0.905	0.220	0.944	0.220
Be	0.170	0.955	0.170	0.994
Pb	0.955	0.170	0.994	0.170
FeB	0.895	0.230	0.934	0.230
FeB	0.835	0.290	0.874	0.290

When analyzing the data recorded at 93 K with the software *ENVI 4.4*, there were two significant peaks that appeared almost allover the recorded image. Fig. 28 illustrates the photoluminescence spectra for both silicon and defects. The data was collected from an area in the wafer where these three peaks occurred simultaneously.

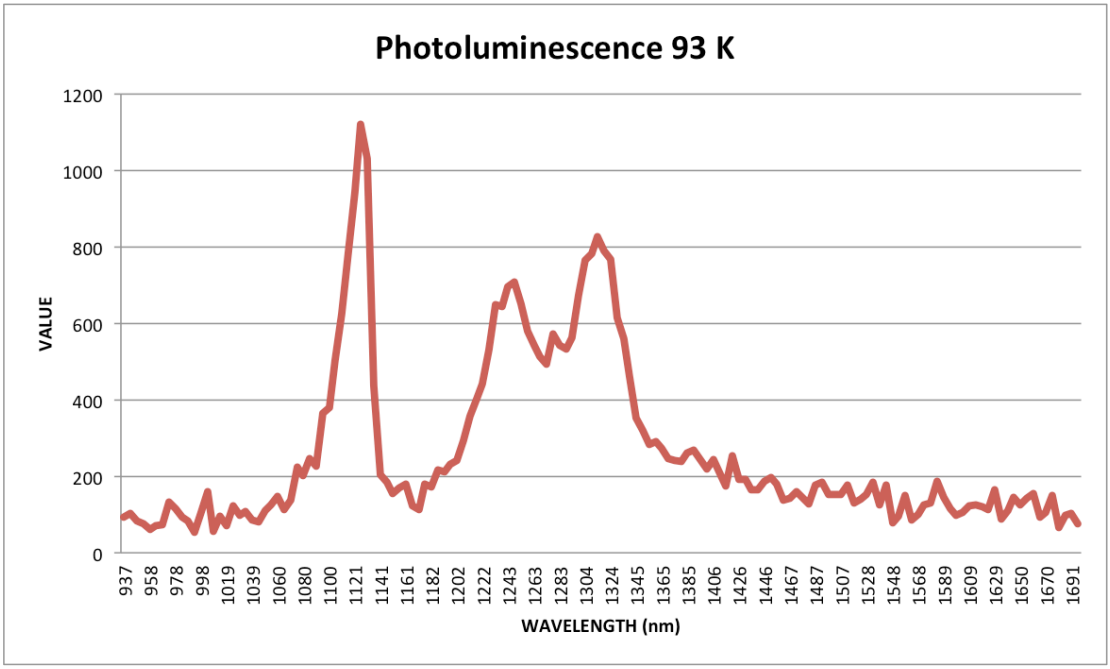

Figure 28: The photoluminescence spectra detected at 93 K for both silicon and defects. The data is collected from an area in the wafer these three peaks occurred simultaneously. The first peak is the green area, the second peak is the blue area and the third area is the red area in Fig. 29.

The peaks have been given different colors so that they could be identified in the photoluminescence image. The photoluminescence image in Fig. 29 is the recorded *raw* image created in the ENVI program.

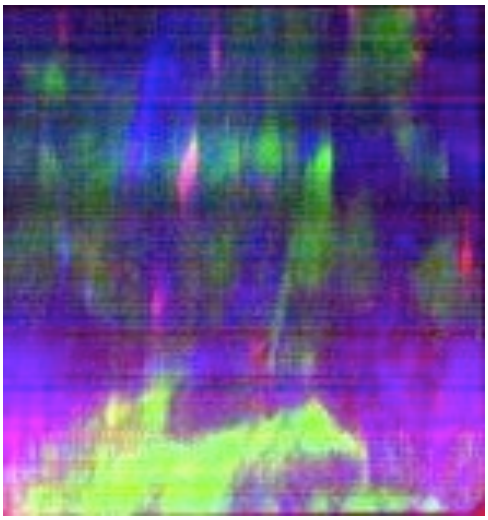

Figure 29: Image from the ENVI program, raw image.

The first peak in Fig. 28 corresponds to the green area found in Fig. 29. The second and third peak is viewed as blue and red, respectively in Fig. 29. The two peaks are known from literature and according to [26] these are known as dislocation features D_1 and D_2. It is not for certain that they are caused by dislocation so they are only denoted as features. Feature D_1 has its peak value at approximately wavelength 1234 nm with the corresponding energy 0.998 eV. Feature D_2 has its peak at wavelength 1314 nm with the corresponding energy 0.944 eV. These are the same peaks as [26] found. From [26] the D_2 line is considered a duplicate of the D_1 line. The correlation between them is displayed in Fig. 29 as the purple area. Thus, the spatial correlation between the two is assumed continuous over the whole wafer. However, sometimes the correlation seems to be violated when one of the peaks exceeds the value (intensity) of the other. This could be because the photoluminescence signal at some points in the wafer are from particular elements with exactly the energy level of one of the peaks. In general, these two peaks in some extent always exist at the same time.

The reason why defect photoluminescence is detectable at low temperatures is discussed at the end of section 4.3.3.

4.3.3 Different defect photoluminescence occurrences

In this section the detected photoluminescence from defects are illustrated by using ImageJ. From the montage, Fig. 21, the appearance of defect photoluminescence was detected throughout all bands of lower energy than the occurrence of photoluminescence of silicon. The images in this section are created over a determined wavelength range. The wavelength range was determined from the analysis of the stack. The stack included all 150 bands recorded. The bands that had similar occurrences were added together to make the detected photoluminescence from defects more evident.

The first occurrence appears from band 57 to band 65, with the corresponding wavelength range 1222nm – 1263 nm and energy range 1.015 eV – 0.982 eV. This occurrence is the first change in the photoluminescence signal detected in the montage from other than silicon. This energy range is the same as the energy rage for first feature, D_1, found in Fig. 28. In these bands the photoluminescence shifts from being from silicon to the dark areas in Fig. 22. Fig. 30 illustrates the image created when all bands from 57 to 65 are added together. To make the characteristics in the image clearer, the contrast is enhanced and the result is displayed in Fig. 31.

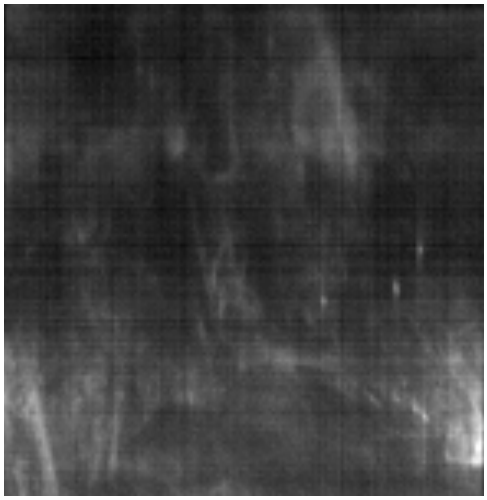

Figure 30: Defect photoluminescence detected from band 57 to band 65. All bands added together.

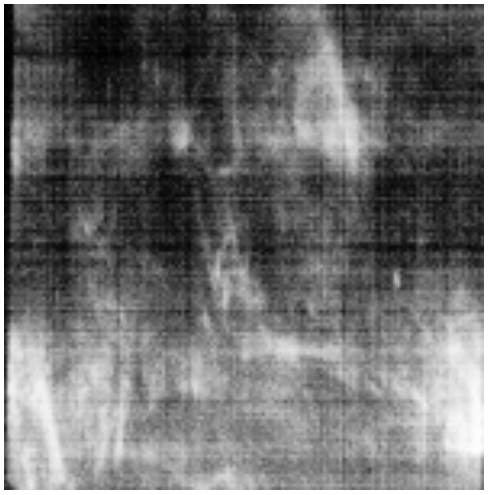

Figure 31: Enhanced contrast of Fig. 30 to enhance the detected features.

The bright areas do not seem to be from specific spots or grains, but smeared out. It is possible that this area consists of many different defects such as clusters or areas of large dislocation structures such as dislocation networks. Fig. 30 is compared with Fig. 22 to illustrate the different detected photoluminescence signals.

Figure 22: Photoluminescence image of silicon recorded at 93 K.

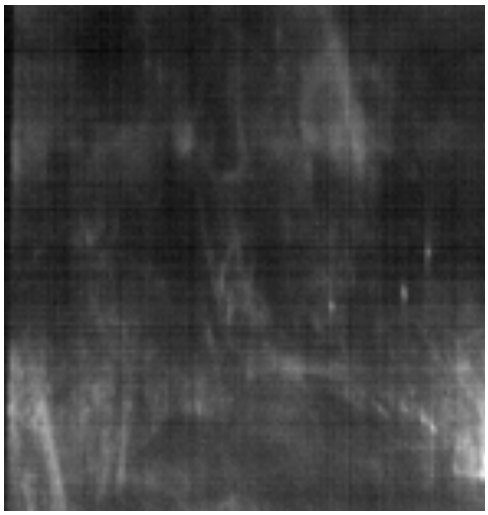

Figure 30 Defect photoluminescence detected from band 57 to band 65.

When comparing the two images above the detected defect photoluminescence signal is clearly not from the same area as the photoluminescence signal of silicon. The same as Fig. 28 shows, the peaks occur at different wavelengths. Also, the blue and purple areas found in Fig. 29 are similar to the bright areas detected in Fig. 30. There are three spots appearing to the right in Fig. 30 in this wavelength range. From the montage, Fig. 21, the spots seems to become visible in band 63. For the photoluminescence signal detected from band 57 to band 65 there are several elements in Table 4 that introduce energy

levels within the band gap in this energy range. Those elements are oxygen (O) with an energy level of 1.004 eV from the valence band, beryllium (Br) with an energy level of 0.994 eV from the conduction band or lead (Pb) with an energy level of 0.994 eV from the valence band.

The second occurrence appears from band 66 to band 80 with the corresponding wavelength range 1268 nm – 1339 nm and energy range 0.978 – 0.927 eV. This occurrence follows the first occurrence. This is the same energy range as the second feature, D_2, found in Fig. 28. All bands in this wavelength range are added together to illustrate all spectral features detected in the same image. Fig. 32 is the image of the sum of all bands from 66 to 80. To make the characteristics in the image clearer, Fig. 33 shows the enhanced contrast of the summed image.

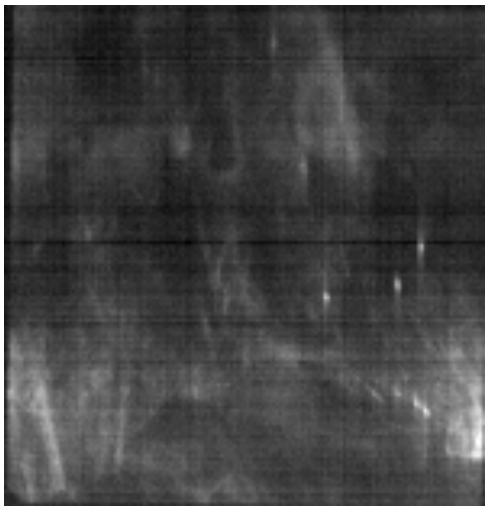

Figure 32: Defect photoluminescence detected from band 66 to band 80. All bands added together.

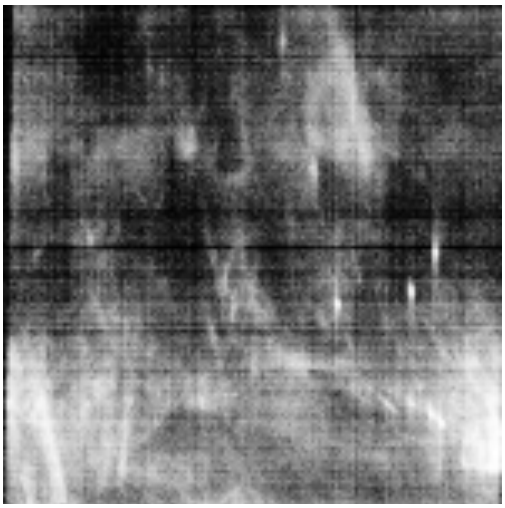

Figure 33: Enhanced contrast of Fig. 30 to see the detected features clearer.

These images reveal the same bright area as found in the first occurrence and the same spots are evident. Defect clusters or dislocation structures such as dislocation networks in the wafer could explain the bright areas in Fig. 32. The difference is that the evident spots are brighter in Fig. 32 than in Fig. 30. Since both Fig. 30 and Fig. 32 have some of the same features this could explain the correlation between feature D_1 and feature D_2. The only thing that separates these two images is the occurrence of bright spots. To take a closer look at these spots, Fig. 30 is subtracted from Fig. 32. The difference between these two images is shown in Fig. 34.

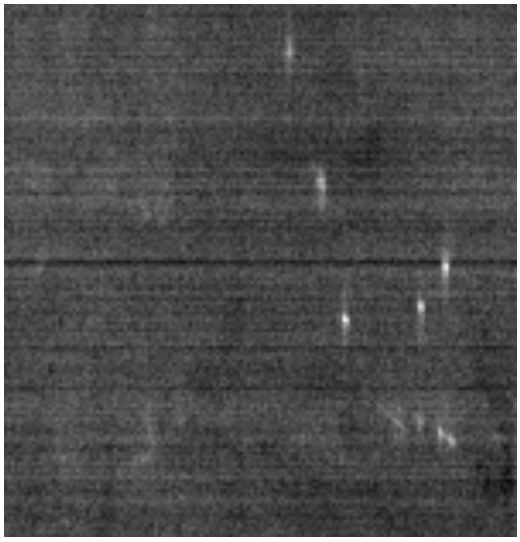

Figure 34: The difference between Fig. 30 and 32. Illustrates the detected bright spots.

The bright spots are displayed in Fig. 34. The bright spots appear in the energy range 0.990 eV to 0.927 eV. It is believed that these bright spots come from point defects such as metal impurities incorporated in the silicon crystal interstitially. The different elements that can occur in this energy range, given those in Table 4, could be either chromium (Cr) with an energy level of 0.944 eV from the valence band, nickel (Ni) with an energy level of 0.944 eV from the conduction band, vanadium (V) with an energy level of 0.944 eV from the valence band or iron-boron-pair (FeB) with an energy level of 0.934 eV from the valence band.

The third occurrence appears from band 81 to band 118 with the corresponding wavelength rage 1345 nm - 1533 nm and energy range from 0.922 eV - 0.809 eV. This occurrence stands out from the first two. In this energy range the detected photoluminescence are from both spots and grains. Still, there are detected some of the same bright areas as the other occurrences though more specific characteristics are detectable. Since the D_2 peak gradually decreases into this energy range, it could explain the still occurring bright area detected in Fig. 35. The characteristic features in this wavelength range are illustrated in an image composed of all the bands from 81 to 118. Fig. 35 is the image created when all bands from 81 to 118 are added together. Fig. 36 shows the spectral features in Fig. 35 clearer by the use of unsharpen filter.

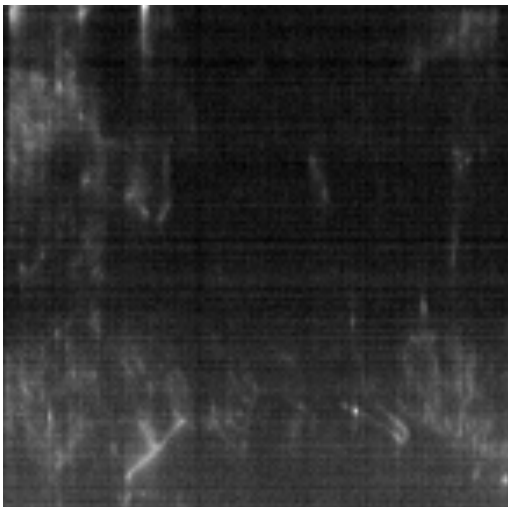

Figure 35: Defect photoluminescence detected from band 81 to band 118. All bands added together.

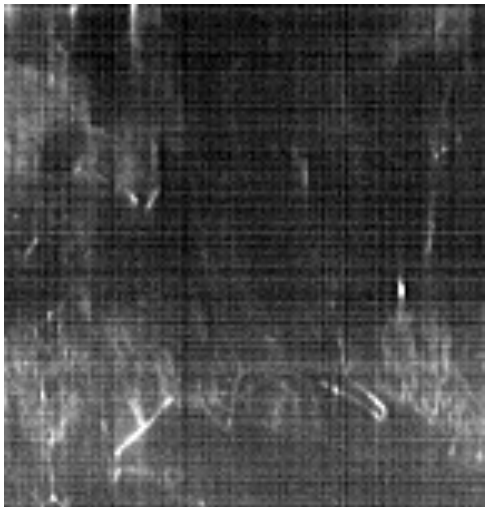

Figure 36: Unsharpen filter used on the image in Fig. 35 to enhance features.

Fig. 35 reveals that the detected photoluminescence signal is from what seems to be both grains and spots, which some are located at the same area. Could also come from dislocation clusters. The area down to the right, which looks like a y, is visible through a wide wavelength range with the strongest signal detected from bond 110 to 118. To see where these features are located in the wafer, Fig. 35 is compared with Fig. 22.

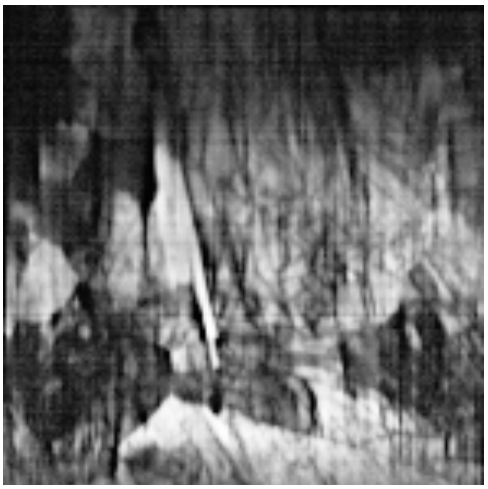

Figure 22: Photoluminescence image of silicon at 93 K.

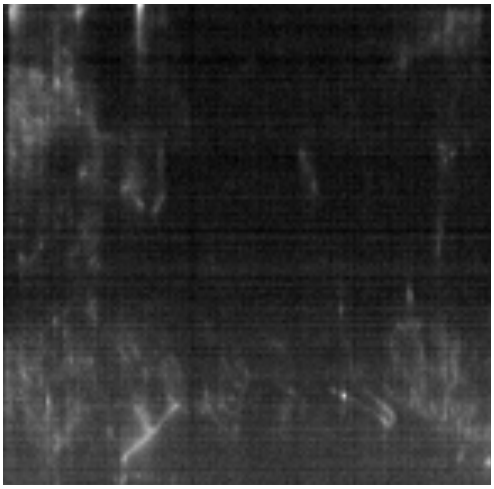

Figure 35: Defect photoluminescence detected from band 81 to 118.

When comparing these two images it is evident that these grain-like formations lies at the edge of the areas where the photoluminescence signal from silicon occur. The most evident signal in Fig. 35 is the bright grain like formations. From Table 4 there are different elements that could explain the detected photoluminescence in this energy range. Those elements are either vanadium (V) with an energy level of 0.864 eV from the conduction band, copper (Cu) with an energy level of 0.924 eV from the conduction

band, iron (Fe) with an energy level of 0.890 eV from the valence band, nickel (Ni) with an energy level of 0.814 from the valence band, manganese (Mn) with an energy level 0.914 eV from the conduction band, chromium (Cr) with an energy level of 0.584 eV from the conduction band, cobalt (Co) with an energy level of 0.814 eV from the conduction band, iron-boron pair with an energy level of 0.874 eV from the valence band or two energy levels introduced by titanium (Ti) of 0.904 eV from the valence band and 0.864 eV from the conduction band.

The forth occurrence appears from band 119 to band 140, with the corresponding wavelength range 1538 nm – 1645 nm and energy range 0.807 eV – 0.754 eV. In this energy range the photoluminescence are also detected from spots, grains and dislocation clusters. The same grain structures as revealed in the third occurrence are also detectable in Fig. 37. The difference is the appearance of more bright spots in the image. Fig. 37 is the image created when all bands from 119 to 140 are added together. Unsharpen filter is used on the image in Fig. 37 to enhance the detected spectral features and this image is displayed in Fig. 38.

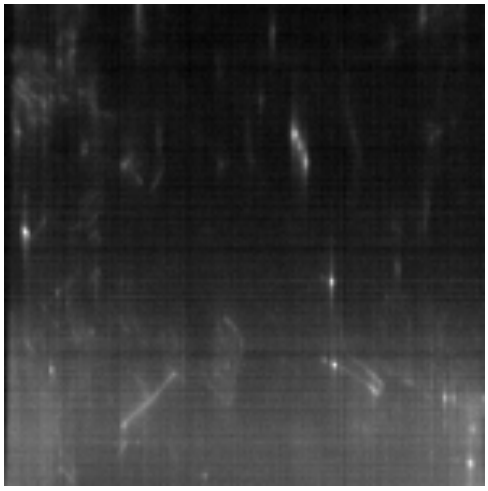

Figure 37: Defect photoluminescence detected from band 119 to band 140. All bands added together.

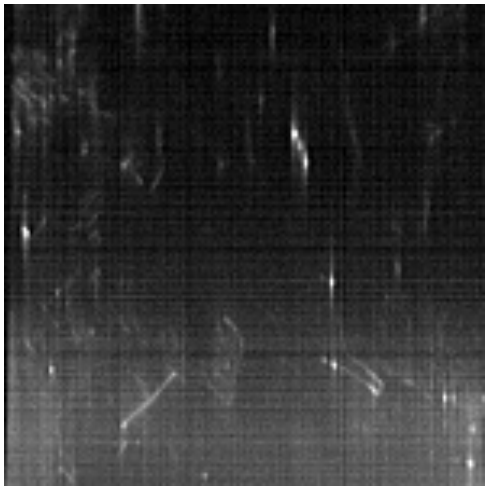

Figure 38: Enhanced contrast of Fig. 37 to see the features clearer.

The visible grains, spots and/or dislocation clusters that occur in this wavelength range could be explained by different elements. Given those in Table 4, the detected photoluminescence could come from either chromium (Cr) with an energy level of 0.754 eV from the valence band, iron (Fe) with an energy level of 0.764 eV from the conduction band, copper (Cu) with an energy level of 0.764 eV from the conduction band or oxygen (O) which introduce two energy levels; one at 0.754 eV from the conduction band and one at 0.784 eV from the valence band.

The fifth occurrence appears from band 141 to band 150, with corresponding wavelength range 1650 nm – 1696 nm and energy range 0.752 eV – 0.732 eV. In this energy range there are several significant bright spots appearing in the image. All bands from 141 to 150 are added together and this image is illustrated in Fig. 39.

Figure 39: Defect photoluminescence detected from band 141 to band 150.

Fig. 40 is the surface plot of Fig. 39. By using surface plot for illustration, it is easier analyze the location, size and intensity of the spots.

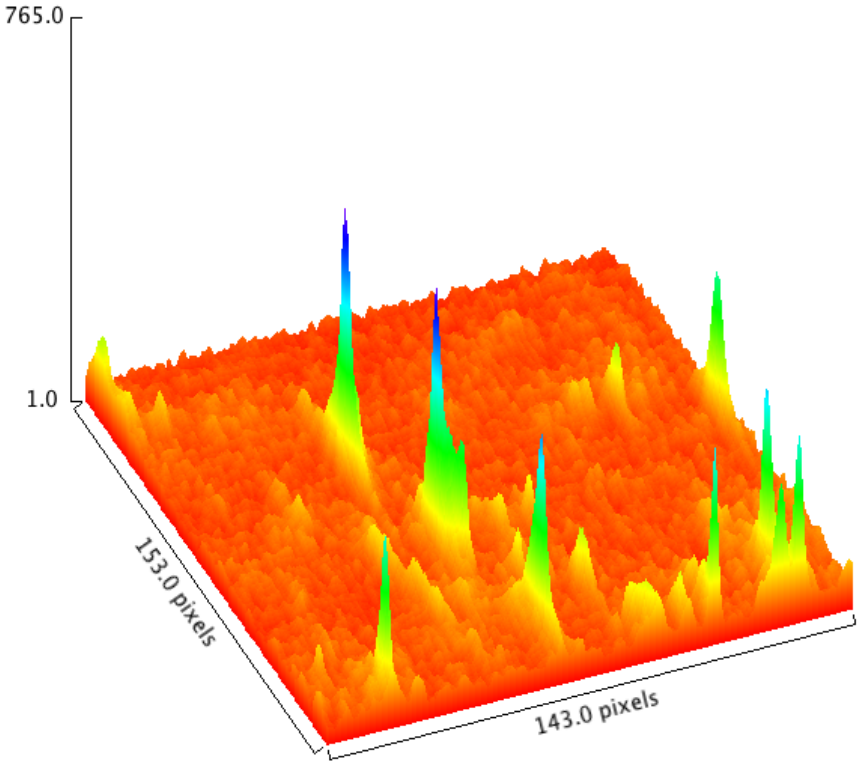

Figure 40: Surface plot of the image in Fig. 39. The vertical axis is the intensity and the two other axes show the location of the spots in the wafer.

From the surface plot there is a strong indication that most of the impurities in this wavelength range are located at the edge of the wafer, segregated along the grain boundaries or form clusters. The strongest signal is detected almost at the center of the wafer. The elements that could cause the photoluminescence appearances in Fig. 39 in this wavelength range, given those in Table 4, are aluminium (Al) with an energy level of 0.734 eV from the conduction band, manganese (Mn) with an energy level of 0.744 eV from the valence band.

The reason why defect photoluminescence is detectable at low temperatures is due to the change in properties of the semiconductor material. As mentioned earlier the size of band gap is temperature dependent, it increases with decreasing temperature. The distance from the valence band and the conduction band to energy states within the band gap increases when the band gap size increases. As a consequence the emitted energy from recombination through these states will be higher at 93 K. The increase in energy level may also result in lower wavelengths detectable for the camera.

At high temperatures, 300 K, excess carriers lose some of their energy when interacting with phonons or become scattered by ionized acceptor atoms. Minority carriers will recombine non-radiatively through states within the band gap and hence will not be detected by the camera. While at low temperatures the density of phonons available for interaction with excess carriers decreases. Still, for momentum conservation the electron-phonon interactions occur since this is an indirect semiconductor. The probability for minority carriers to recombine through states in the ban gap increases with decreasing temperature. This is due to two mechanisms: 1) Less phonon-electron interaction. 2) Low enough temperature to discourage thermal activation of carriers out of traps. Thus, electrons recombine through defects radiatively.

Electrons are allowed to move more slow and longer in the material before recombining due to less phonon-interaction and ionized impurity scattering. Not all impurities are ionized at low tempeteratures. At 93 K the ionization factor is approximately 60 %, which means that 40 % of the acceptor atoms are “freezed-out”. Since ionized impurities scatter electrons more effective than non-ionized, this scattering mechanism is also reduced at low temperatures. The carrier lifetime increases since the electrons will reside in the conduction band for a longer period. The shallow levels introduced by acceptor atoms, which are partially occupied at low temperatures, allow effective

recombination. The probability of recombining through them increases upon decreasing temperature. The essence is stat the probability for detecting defect photoluminescence increases with decreasing temperature due to the behavior of excess carriers.

Since excess carriers remain in the conduction band longer and they move more slow and further, the probability of electron diffusion to grain boundaries increases. Grain boundaries are the most limiting factor for the efficiency of the solar cell. Excess carriers recombine radiatively through energy levels introduced by the impurities in the grain boundaries at 93 K. This is why photoluminescence from grains are detectable by the camera at low temperatures. These grains have different formations than those found in the photoluminescence image in Fig. 22. They could be defect clusters that form small angle grain boundaries in the wafer. The emitted energy from recombining through states is characteristic for the location of each state in the band gap. Thus, the specific element that introduces the state in the band gap can be identified.

The different occurrences mentioned earlier in this section are chosen for their spectrally characteristic feature through several bands. Even though there are some different characteristic features within the chosen *occurrences* they explain mostly the same. The element analysis of the occurrences is based on the different energy levels that each element introduces within the forbidden band gap. No specific identification of the elements detected is given because it would have been inaccurate. From this method with such varying results, the element analysis only results in assumptions made for each occurrence.

4.3.4 3D visualization

3D visualization of the recorded data at 93 K is used for the presentation of the dataset. When viewing all spectral bands in 3D it is possible to visualize the location of different elements incorporated in the wafer. Fig. 41 illustrates the change in photoluminescence signal detected in bands ranging from 35 - 148. The images in Fig. 41 display the 3D plot from different angles for presentation. The first 34 bonds were removed from the stack before building the 3D model because they did not include any detected photoluminescence. The area in Fig. 41 that is squared contains photoluminescence detected from of both silicon and defects. The defect photoluminescence is probably from the defect features describe in the previous section. The protruding lines are assumed to be different elements incorporated in the material.

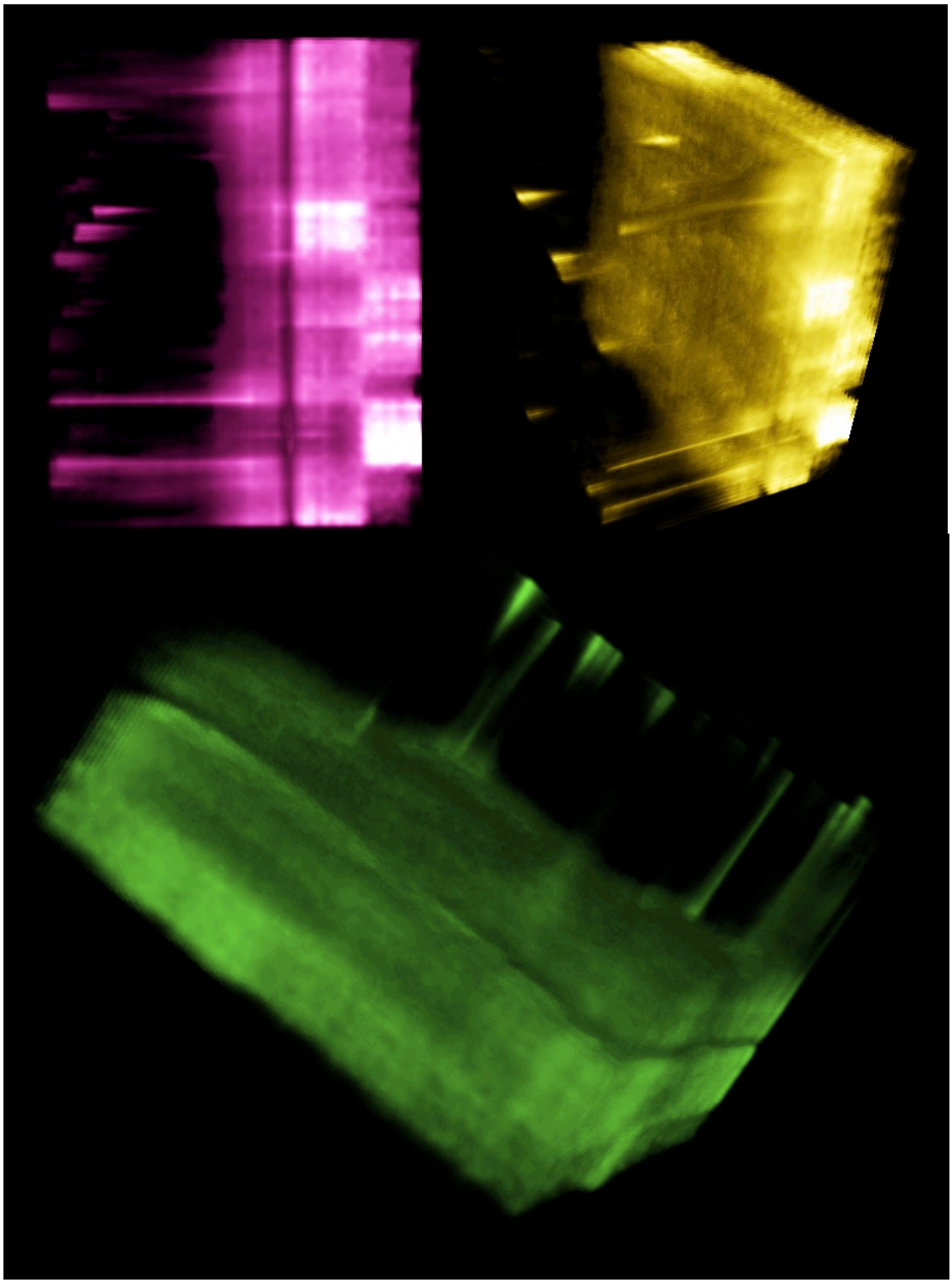

Figure 41: 3D visualization of the dataset recorded at 93 K. The three images are taken at different angles so that most of the characteristic features in the image are visible.

The edge of the solid square start at band number 35 and the edge of the protruding lines end at band 149. This is the wavelength range 1110 nm - 1691 nm. The protruding lines are believed to be different elements incorporated in the material. The solid part of the image is the photoluminescence signal detected from silicon and the areas where the

signal shifts to the dark areas in the photoluminescence image of silicon. In the area of the image were the protruding lines are evident there seems to be no other signal detected, which indicates wither that there is little noise from the recording in this area. When the data is illustrated in a 3D plot it is possible to notice that some of the different elements are present throughout a wide wavelength range. Also it is noticeable that some of the elements are present in the grain boundary regions in the wafer. From the purple image in Fig. 41 it is possible to see that the protruding lines comes from the edge of the area of photoluminescence signal of silicon. From this 3D visualization there is impossible to say anything about what sort of elements that makes up these protruding lines. Thus, this 3D visualization is only useful for illustrating how some of the elements behave throughout a specific wavelength.

4.4 Multivariate image analysis

Principal component analysis was performed on two hyperspectral images recorded at different temperatures, 300 K and 93 K. The principal component analysis is performed on these two datasets to see if the results derived from the montages are in fact photoluminescence of silicon and defects. The principal component analysis is used to enhance particular spatial and spectral patterns found in the dataset. The principal component analysis transforms these large datasets into a number of principal components. Each component is illustrated with a score image and a loading plot. The principal component analysis finds the components in a decreasing order of importance. Each component image is also displayed as enhanced contrast for interpretation and presentation. The variables in these datasets are wavelengths ranging from 937 nm in band 1 to 1696 nm in band 150.

4.4.1 Principal component analysis on image recorded at 300 K

The number of principal components chosen for the model is based on how much of the variation in the dataset each component explains. How many percent the components explain of the cumulative variance captured by the model are illustrated in Fig. 42. Fig. 42 is a plot of the cumulative variance captured as a function of the number of principal components retained in the model for this principal component analysis.

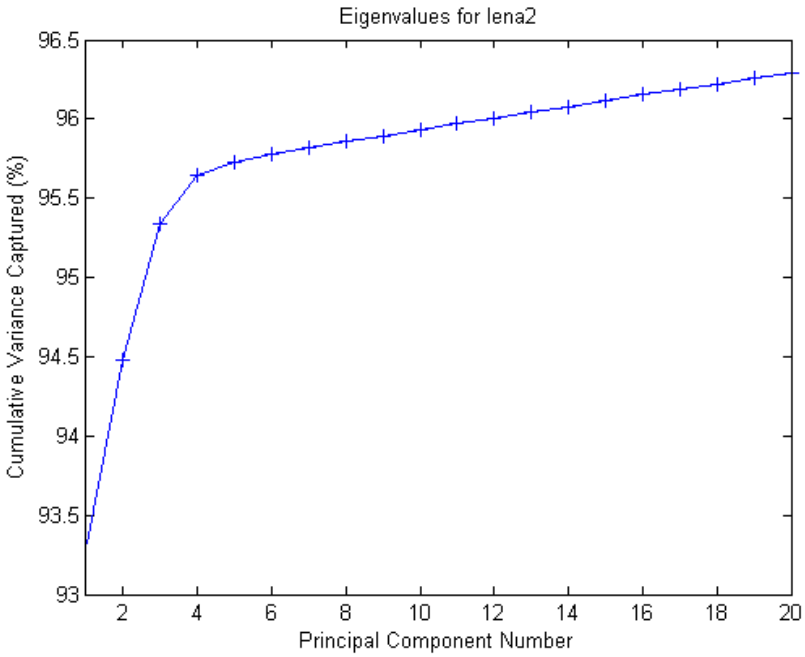

Figure 42: Plot of the cumulative variance captured as a function of the number of principal components retained in the model for this principal component analysis.

From Fig. 42, the first principal component explains 93.3 % of the cumulative variance captured by the model and the second component explains 94.5 %. Since there is only a small difference in percentage between them, the second component does not include any new or interesting information about the variation dataset. Therefore the only principal component in this analysis is the first one.

The first principal component explains the greatest variation in the dataset. This principal component explains particular spectral features in the original image. The score image illustrates the image of these particular spectral features, and the loading plot contains information about the variables.

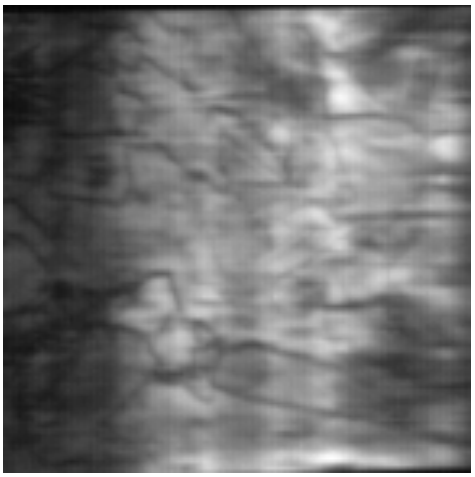

Figure 43: Score image of the first principal component.

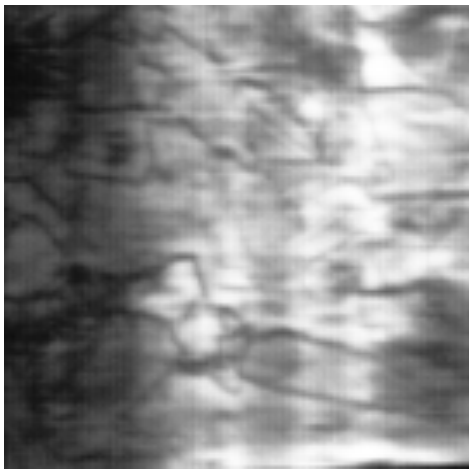

Figure 44: Enhanced contrast of the score image.

Fig. 43 is the score image of the first principal component and Fig. 44 is the enhanced contrast of the score image. Fig. 45 is the loading plot. The loading plot reveals which variables (wavelengths) that explain the spectral features of the score image. It is the strength of the loadings that decides how much they explain in the score image.

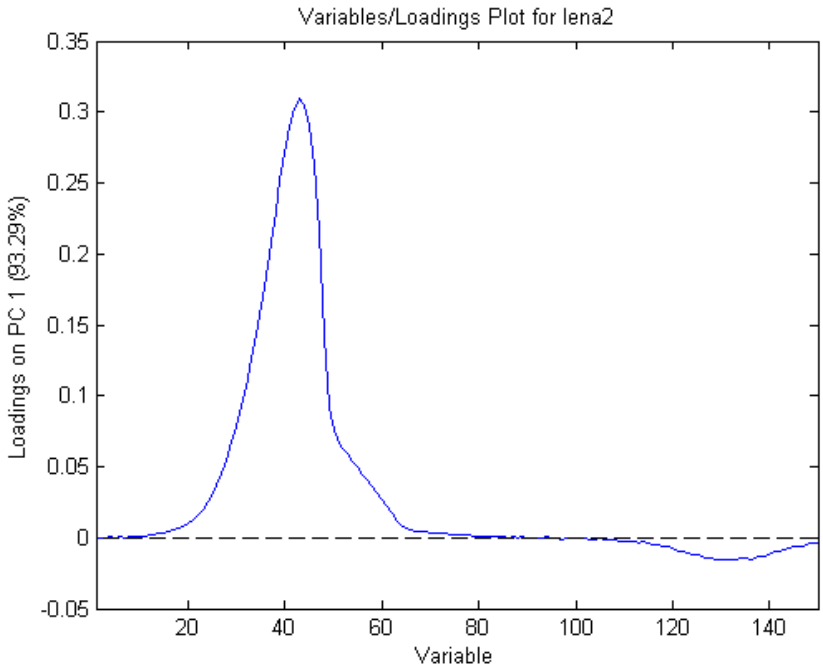

Figure 45: Loading plot of the first principal component. The loading plot describes the spectral features (variables) in the score image.

The score image in Fig. 43 is very similar to the photoluminescence image of silicon from section 4.2.1, Fig. 16. Fig. 16 is the image created when all the bands the most evident photoluminescence image of silicon are added together. The spectral information found in the loading plot, Fig. 45, is the same found in the Fig. 20, the photoluminescence spectrum of silicon at 300 K. From this, it is possible to assume that 93.29 % of the variation of the recorded dataset is explained by photoluminescence detected from silicon. The shoulder on the silicon peak is due to phonon-interactions. The negative loading value of the peak that occurs from band 120 to 140 also explains some of the spectral features found in the score image. This curve could explain the dark areas in the score image. It is the strength of the loading that determines how much they explain in the score image and their value, negative or positive, does not necessarily explain bright or dark areas in the image. The principal component analysis reduced the large dimensionality of the dataset to one principal component that explained most of the variation in the dataset. And this, not unexpected, was the photoluminescence image of silicon. This analysis and the montage revealed the same information.

4.4.2 Principal component analysis on image recorded at 93 K

The number of principal components chosen for the model is based on the percentage each component explains of the cumulative variance captured by the model. Fig. 46 is a plot of the cumulative variance captured as a function of the number of principal components retained in the model for this principal component analysis.

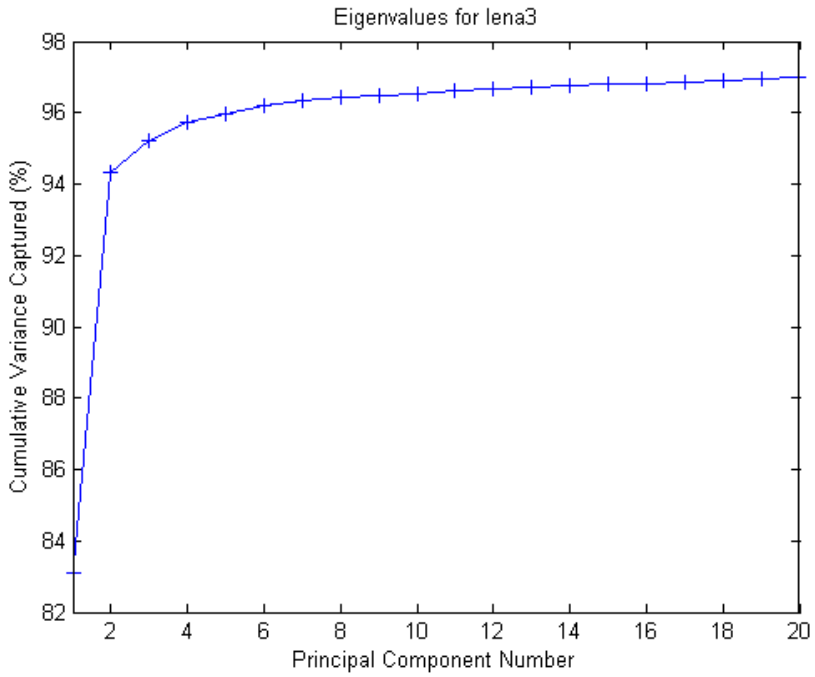

Figure 46: Plot of the cumulative variance captured as a function of the number of principal components retained in the model for this principal component analysis.

Fig. 46 reveals that the first two principal components explain 94.3 % of the cumulative variance captured by the model. After the second component there is little increase in percent that is explained by the rest of the components. Therefore the large dataset is only reduced to two uncorrelated principal components. The two components are illustrated and explained in this section with a score image and a loading plot. The two principal components explain particular features that occur in the original image.

The first principal component explains the greatest variation in the dataset. The score image illustrates particular spectral features and the loading plot contains information about the variables that explains these spectral features. The score image is enhanced to display the spectral features clearer.

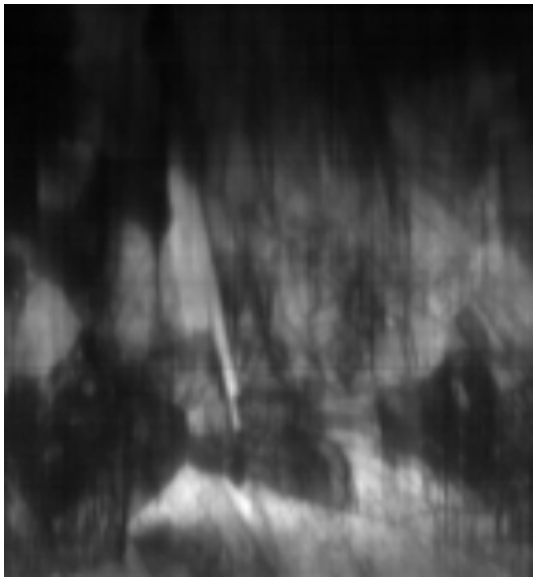

Figure 47: Score image of the first principal component.

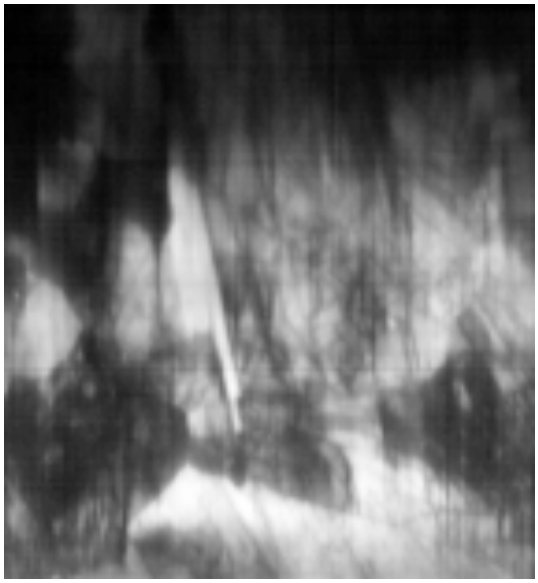

Figure 48: Enhanced contrast of the score image in Fig. 47.

Fig. 47 is the score image and Fig. 48 is the enhanced contrast of the score image. Fig. 49 is the loading plot. The loading plot reveals which variables (wavelengths) that explain the spectral features detected in the score image. It is the strength of the loadings that decides how much they explain in the score image.

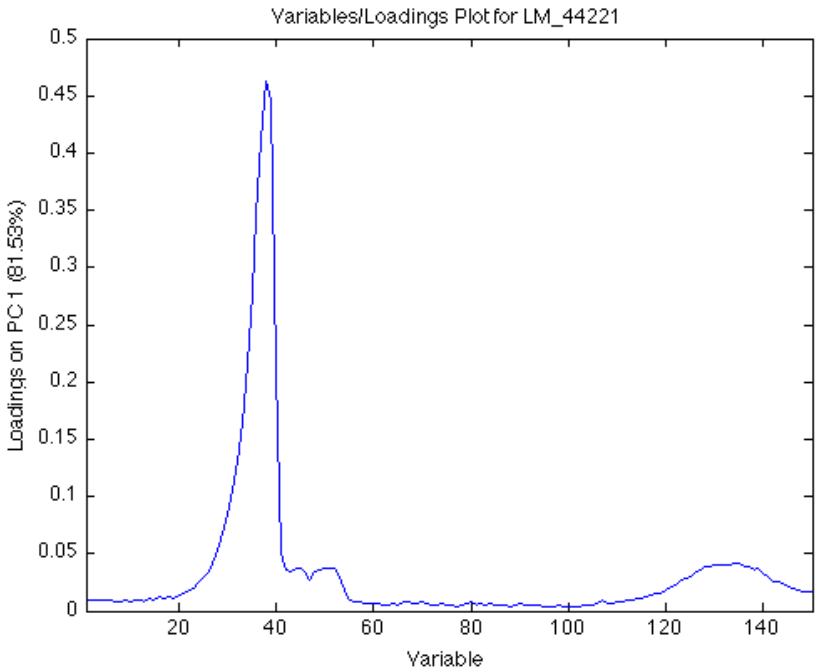

Figure 49: *Loading plot of the first principal component. The loading plot describes the spectral features (variables) in the score image.*

The spectral features in the loading plot consist of two significant peaks. The first peak start at variable 25 and end at 40 where it is accompanied by a shoulder. The second

peak occurs from variable 118 to 150. Both peaks show which variables that explain the score image. The score image resembles the photoluminescence image of silicon in Fig. 22. The spectral feature of the first peak found in the loading plot is the same as the photoluminescence spectra of silicon detected at 93 K, illustrated in Fig. 26. The loadings plot reveals that the variables, i.e. spectral bands, 30 – 40 explain most in this score image. This is the same as the photoluminescence spectra of silicon with a wavelengths range 1085 nm - 1136 nm. The shoulder from band 40 - 57 is an effect of the phonon-electron interaction. The phonon-interaction is temperature dependent and explained in section 4.2.1. 81.53 % of the spectral feature in the data set is explained by the appearance of photoluminescence of silicon and the additional small peak at longer wavelengths. The first principal component reveals the photoluminescence image of silicon.

The second principal component explains the second greatest variation in the dataset. The score image illustrates the particular spectral feature and the loading plot contains information about the variables that explains this spectral feature.

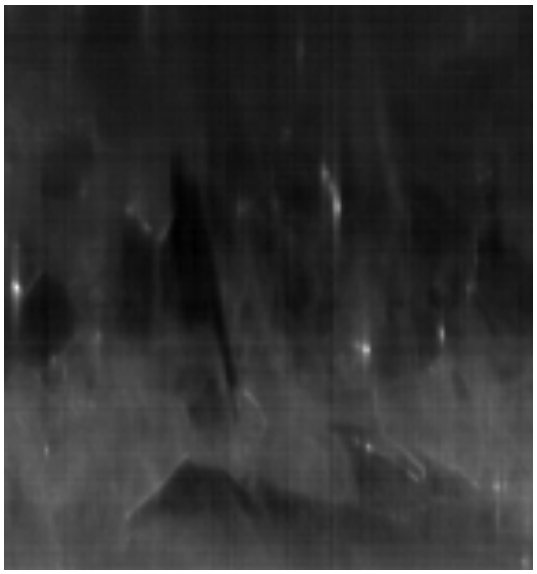

Figure 50: Score image of the second principal component.

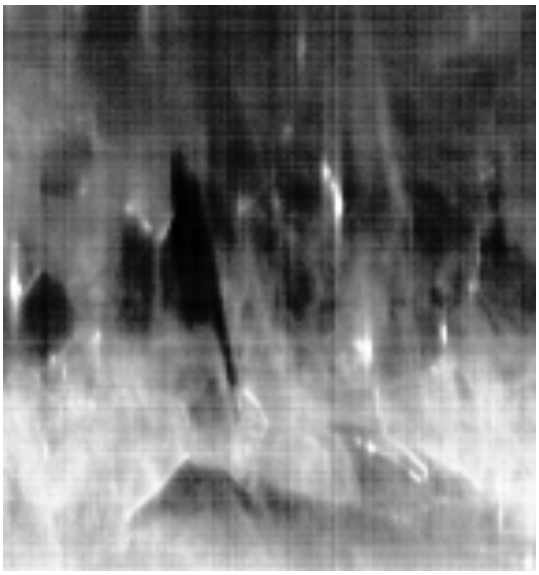

Figure 51: Enhanced contrast of the score image in Fig. 50.

Fig. 50 is the score image of the second principal component. Fig. 51 is enhanced contrast of the score image. When enhancing contrast of the score image, the spectral features detected in the image become more evident. Fig. 52 is the loading plot, which illustrates which variables that explain the spectral features found in the score image in Fig. 50.

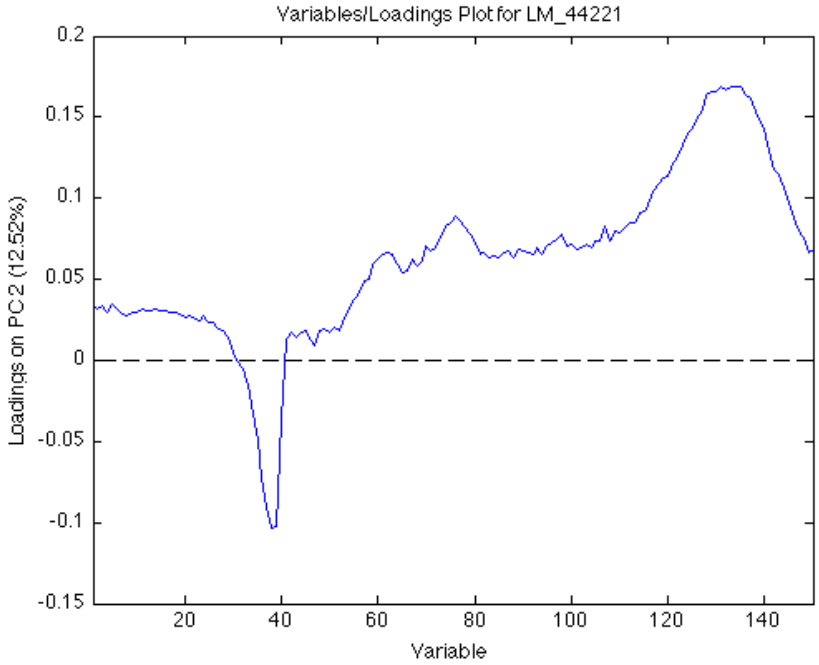

Figure 52: Loading plot of the second principal component. The loading plot describes the spectral features (variables) in the score image.

Fig. 52, the loading plot, shows that the second principal component explains 12.52 % of the variation in the dataset. There are four significant peaks that occur in this loading plot, which explains the features in the score image. The first peak is the same as detected in the first principal component except that it has negative loading values. The first two positive peaks appear from variable 57 to 80. The third positive loading peak occurs from variable 118 to 150. Since the variables are wavelengths, these peaks explain the different spectral features found in the score image. The first peak is expected to be the silicon spectra, and from Fig. 52 this spectrum explains some of the features in the score image. This peak could explain the areas that appear dark in Fig. 52. The shoulder caused by the phonon-interaction is also detected in Fig. 52. The two peaks from variable 57 to 80 are expected to be the spectral features D_1 and D_2, described in section 4.3.2. The score image reveals some of the same features found in the montage in Fig 21. The last peak is twice as large as the D_1 and D_2 peaks. This indicates that the defects detected in this wavelengths range in the montage of Fig. 21 describes more of the variation the dataset that the rest of the defects detected. The second principal component reveals the defect photoluminescence in one image. The score image, Fig. 50 reveals most of the defects found in the montage, Fig.21. Which means that photoluminescence of silicon explains 81.53 % of the variation in the dataset, while defect photoluminescence explains 12.52 % of the variation the dataset.

The two principal components are uncorrelated and reveal both the same and different spectral information in the dataset. Fig. 53 illustrates the two loading plot in the same figure.

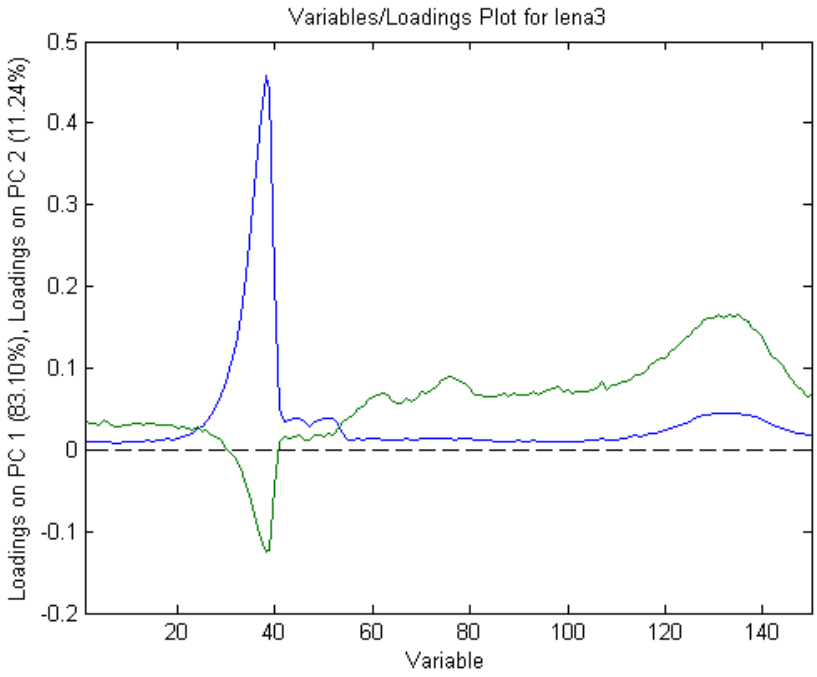

Figure 53: Loading plot of the first and second principal component plotted together.

Fig. 53 shows the spectral features of the two principal components in one plot. They are plotted together to make it easier to illustrate at which variables they describe the same features or not. The peak assumed to be the spectrum of silicon is found in both principal components. This can either be because photoluminescence of silicon is detectable in both score images, or it could explain that the dark areas in the second score image is the area of silicon. The latter is most likely to be the explanation, since these are in fact the areas that occur bright in the photoluminescence image of Fig. 22. The two peaks that only occur in the loadings of the second principal component are similar to the features D_1 and D_2 described in section 4.3.2 and displayed in Fig. 29. The third peak is detectable in both principal components, but at a different extent. The loading value of the third peak is greater in the second component, which means that this explains more of the spectral features in the score image of the second principal component than in the first. This peak could also explain the defect photoluminescence detected from band 118 – 150 in section 4.3.3.

From the principal component analysis of these datasets it is evident that photoluminescence from silicon and defects are the spectral features detected.

4.5 Measurement errors

We can assume that there might be measurement errors associated with the imaging techniques that is used for photoluminescence detection. For instance, these errors could arise from calibration, temperature variations of the surroundings and human inaccuracy.

Across the laser beam the intensity of the laser varies, this will have a significant impact on the resulting images. Especially in Fig. 16 and 22 the effect is detectable, some areas clear while others are diffuse and dark. This effect is expected because the semiconductor making up the laser is in general very uneven.

The dark bands detected in the montages are results of "bad" pixels. They are either found as completely dark images or with a bright line through the black image. The bad pixels are found in different bands, mostly in band 19, 47 and 107. Thus, it is assumed that they did not affect the results that are shown in this thesis. It seems that the number of "bad" pixel increases with increasing closing time. They could also be an effect of a poor background recording, if the camera entrance was not completely covered by a black object.

When using liquid nitrogen to freeze the sample, it is important to avoid the surrounding air to react with the cold air inside the vessel. When the glass lid is removed from the cryogenic vessel during recording, there is only a short period of time before water vapor occurs on the wafer. They form frost on the wafer, which will decrease the intensity of the photoluminescence signal. The wafer has to be removed after every recording to avoid biased results.

If the filter is not placed properly underneath the camera lens this cause a small clearing this can result in second order refraction, which will largely affect the results. This effect will be noticeable at approximately 1600 nm.

When the cryogenic vessel is filled with liquid nitrogen the metal contracts. Since the distance between the camera and laser and wafer is calibrated before freezing process, this contraction can result in a change in focal point. This can affect the recording and make blurred images.

5. Conclusion

Defects such as impurities, grain boundaries and dislocations structures introduce different states within the forbidden band gap of silicon. The quasi-steady-state photoconduction measurement supported the assumption that the multicrystalline silicon wafer examined in this thesis actually contained a large density of defects. To investigate inter band gap photoluminescence the wafer was examined at two different temperatures. The photoluminescence detected at 300 K was solely from silicon. Inter band gap photoluminescence were not detected at 300 K since non-radiative recombination through states within the band gap is the dominant recombination route. There are two mechanisms that cause the non-radiative effect: 1) Electron-phonon interactions. 2) To high temperature to discourage activation of carriers out of traps. At 93 K both inter band gap photoluminescence and photoluminescence of silicon were detected. The detected photoluminescence signal of silicon at 93 K was stronger but spectrally narrower than at 300 K. The multi-phonon interaction is temperature dependent and affects the photoluminescence signal. Inter band gap photoluminescence were detectable at low temperatures due to the radiative activation of energy levels within the band gap. At 93 K there are less phonon-electron interaction in the material and the thermal activation of carriers out of traps occurs. Thus, when electrons recombine through states within the band gap they emit photons with a specific wavelength. This allows the impurities that introduce the state to be identified from the photoluminescence spectrum. The grain boundaries detected in the photoluminescence image of silicon at 93 K were narrower than at 300 K, this is due to the larger quantity of electrons that diffusion to the grains where they recombine. The features D_1 and D_2 were detected at 93 K and in addition there were detected defect photoluminescence in an even lower energy range. The inter band gap photoluminescence images revealed spectral features from dislocations, grains and point defects. The principal component analysis that were performed on the recorded datasets from 300 K and 93 K revealed that the photoluminescence occurrences found in the montage was in fact photoluminescence from silicon and different defects. From the photoluminescence imaging technique applied in this thesis, inter band gap photoluminescence was detected when the wafer was examined at 93 K. At 300 K the applied technique was not able to detect the defects found at 93 K. This indicates that temperature is a key factor when examining the wafer for defects when using the photoluminescence imaging technique. Furthermore, this technique has proven to be a fast and nondestructive method for defect investigation in multicrystalline silicon wafers.

6. Further research

The fact that defect photoluminescence was detectable with the photoluminescence mapping technique used in this thesis provides many possibilities for further research.

Due to the effect the laser had on the results, a new and less uneven laser should replace the existing laser and this will probably improve the results. This could be either a stronger or weaker laser. They could be used for excess carrier concentration investigation at different laser intensities and for comparison. Which laser is best for defect analysis?

It would be interesting to investigate how the photoluminescence spectrum changes with temperature in the range 300 K – 93 K, or lower, and finding out at which temperature defect photoluminescence become detectable. The lowest reachable temperature with liquid nitrogen is 77 K. Using helium instead of nitrogen for the wafer freezing process it is possible to reach temperatures down to 4.2 K.

There were found defect photoluminescence up to 1700 nm and they did not seem to vanish at this wavelength. If replacing the existing camera with another that detects a wider wavelengths range, photoluminescence from more elements might be detectable.

The recorded background has proven to have a significant effect on the recordings taken with different closing time. The technique used for background recording should be reformed. To obtain better results this effect should be investigated further.

A more specific identification of the elements incorporated in the multicrystalline wafer is important for understanding their impact on the semiconductor properties. This requires more steady and reliable results from the photoluminescence mapping technique used today.

7. References

[1] Martin A. Green, *Solar Cells Operating Principles technology and system Applications.* The university of New South Wales (1988).
ISBN: 0-85823-580-3

[2] Eric McLamb, *Fossils Fuels vs Renewable Energy Resources: Energy's Future Today*. http://ecology.com/features/fossilvsrenewalble/fossilvsrenewable.html
Downloaded 20.04.2011

[3] Philipp Rosenits, *Minority carrier lifetime in silicon wafers and thin-film material*. Fraunhofer Institute for Solar Energy Systems (ISE), Freiburg, Germany.

[4] Andreas Bentzen et al, *Recombination Lifetime and Trap Density Variation in Multicrystalline Silicon Wafers Through the Block.* (2005).

[5] Thomas S. Jones, *Silicon*. U.S. Geological Survey Minerals Yearbook, (2000).

[6] Martin C. Schubert et al, *Imaging of metal impurities in silicon by luminescence spectroscopy and synchrotron techniques*.
Journal of Electronic materials, Vol. 39, No. 6 (2010).

[7] William D. Callister, Jr, *Material Science and engineering and introduction*, 7th edition. USA, (2007).
ISBN-13: 978-0-471-73696-7

[8] Eivind Øverlid and Espen Olsen, *Impurities in solar grade silicon and their effect on solar cell performance*. SINTEF REPORT, (2004).
ISBN: 82-14-02201-0

[9] Robert F. Pierret, *Semiconductor device fundamentals*. USA (1996).
ISBN-13: 9780201543933

[10] S. Rein, *Lifetime Spectroscopy: A Method of Defect Characterization in Silicon for Photovoltaic Applications.* Springer-Verlag Berlin Heidelberg (2005).
ISBN: 3-540-25303-3

[11] Scotten W. Jones, *Properties of Silicon*. IC Knowledge LLC, (2008).

[12] Antonio Loque and Steven Hegedus. *Handbook of photovoltaic science and engineering.* England, (2003).
ISBN: 0-471-49196-9

[13] Jasprit Singh, *Semiconductor Devices - basic principles*, chapter 3 *Semiconductor Bandstructure*. www.eecs.umich.edu/~singh
Downloaded 20.04.2011

[14] Richard C. Neville, *Solar Energy Conversion: THE SOLAR CELL*. 2nd edition. Netherlands (1995).
ISBN: 0-444-898182

[15] Jan-Pierre Colinge and Cynthia A. Colinge, *Physics of Semiconductor Devices*. USA, (2006). ISBN: 0-387-28523-7

[16] Daniel H. Macdonald PHD thesis, *Recombination and Trapping in Multicrystalline Silicon Solar Cells*. The Australian National University, (2001).

[17] T. Trupke et al, *Temperature dependence of the radiative recombination coefficient of intrinsic crystalline silicon*. Journal of Applied Physics, Vol. 94, No. 8. American Institute of Physics (2003).

[18] Dinesh C. Gupta et al, *Recombination Lifetime measurements in silicon*. Chelsea, (1998). ISBN: 0-8031-2489-9

[19] K. Graff, *Metal Impurities in Silicon-Device Fabrication*, 2nd edition. Springer-Verlag Berlin Heidelberg New York. ISBN: 3-540-64213-7

[20] Rafael Krain et al, *Low-Temperature Gettering of Iron in Mono- and Multicrystalline Silicon.* Germany, (2009).

[21] L. J. Geerlings and Daniel Macdonald, *Dynamics of light induced FeB pair dissociation in crystalline silicon*. Applied Physics Letters, Vol. 85, No. 22. (2004).

[22] Matthias Demant et al, *Analysis of Luminescence Images Applying Pattern Recognition Techniques*. (2010).

[23] M. Inoue et al, *Microscopic and spectroscopic mapping of dislocation-related photoluminescence in multicrystalline silicon wafer*. J Mater Sci: Mater Electron (2008), 19:S132-S134.

[24] Bhushan Sopori et al, *Performance Limitations of mc-Si Solar Cells Caused by Defect Clusters*. National Renewable Energy Laboratory. USA, (2009).

[25] Timothy H. Gfroere, *Photoluminescence in Analysis of Surface and Interfaces,* in Encyclopedia of Analytical Chemistry. R. A. Meyers (Ed.) pp. 9209-9231, © John Wiley & Sons Ltd, Chichester, (2000).

[26] T. Arguirov et al, *Photoluminescence Study on Defects in Multicrystalline Silicon*. Semiconductors (2007), Vol.41, No. 4, pp. 436-439.

[27] Wai Lek Ng et al, *An efficient room-temperature Silicon-based light-emitting diode*. UK, (2001). *Letters to nature.*

[28] Kateryna Artyushkova and Julia E. Fulghum, *Multivariate Image Analysis and Methods Applied to XPS Image Sets.* Chemistry department, Kent State University, USA (2001).

[29] Barry M. Wise et al, *MIA_TOOLBOX VERSION 1.0,* Eigenvector research, Inc. USA, (2005).

[30] J. F. MacGregor, Multivariate Image Analysis for process monitoring and control. Dep. of Chem. Eng., McMaster University, Hamilton, Ont., Canada L8S 4L7.

[31] Carl Duchesne et al, *Application of multivariate Image Analysis to Predict Concentrate Grade in Froth Flotation Processes.* Otawa, Ontario, Canada (2003).

[32] Internet site for Norwegian Electro Optic AS: *http://www.neo.no/hyspex/ Downloaded 14.03.2011*

[33] Sinton Consulting, Inc. User Manual BCT-400 Photoconductance Tool (2003).

[34] Peg Shippert, Ph. D. *Introduction to Hyperspectral Image Analysis*. Earth Science Apllications Specialist Research Systems, Inc.

[35] Andreas Cuevas et al, Recombination and Trapping in Multicrystalline Silicon. IEEE Transactions on Electron Devices (1998).

8. Appendix

Appendix A

MATLAB functions and programs used in this thesis

1. How to read HYSPEX files in MATLAB

```
function mu = read_HYSPEX_file_all(file)

fid = fopen(file, 'rb');
 start = fread(fid, 8, 'uchar');

% Check if it is a HYSPEX file
if (start(1:8) == [72;89;83;80;69;88;0;0])

% Read header information
   size = fread(fid,1,'int32');
   fseek(fid, 1949, 'cof');
   spectral = fread(fid, 1, 'int32');
   spatial = fread(fid, 1, 'int32');    % # of pixels in y direction
   fseek(fid,4*26,'cof');
   number = fread(fid,1,'int32');   % # of frames or x direction on image
   fseek(fid,size,'bof');
   bands= spectral;                 % Load all spectral bands

   f = zeros(spatial, number);
   mu = zeros(spatial, number, bands);

if (bands > spectral)
      warning('The band number is larger than the number of bands in the file');
      return;
   else
    for j = 1:bands
      fseek(fid, size, 'bof');
      for i = 1:number
         if (i == 1)
            fseek(fid, spatial*(j-1)*2, 'cof');
         else
            fseek(fid, (spectral-1)*spatial*2, 'cof');
         end
            f(:, i) = fread(fid, spatial, 'uint16');
      end
      mu(:, :, j)=f;
    end
   end

else
      warning('Not a HySpex file');
      return;

end
fclose(fid);
```

2. Function for viewing all 150 bands recorded as a movie in MATLAB

```
% The function is based on scripts from Ole Mathis Kruse and Andreas Flø

function [Image] = View_Hyspex_Images(b, from, to )

% The speed of light, m/s
    c = 3.00*10^8;
% Planck's constant, eV * s:
    h = 4.13566743*10^(-15);

    hc = h*c;

%  Defining wavelengths, nm:
     lambdaRaa = [937.438535, 942.527186, 947.615837, 952.704488, 957.793140, 962.881791,
     967.970442, 973.059093, 978.147745, 983.236396, 988.325047, 993.413698, 998.502350,
     1003.591001, 1008.679652, 1013.768303, 1018.856955, 1023.945606, 1029.034257, 1034.122908,
     1039.211560, 1044.300211, 1049.388862, 1054.477513, 1059.566165, 1064.654816, 1069.743467,
     1074.832118, 1079.920770, 1085.009421, 1090.098072, 1095.186723, 1100.275375, 1105.364026,
     1110.452677, 1115.541328, 1120.629980, 1125.718631, 1130.807282, 1135.895933, 1140.984585,
     1146.073236, 1151.161887, 1156.250538, 1161.339190, 1166.427841, 1171.516492, 1176.605143,
     1181.693795, 1186.782446, 1191.871097, 1196.959748, 1202.048400, 1207.137051, 1212.225702,
     1217.314353, 1222.403005, 1227.491656, 1232.580307, 1237.668958, 1242.757610, 1247.846261,
     1252.934912, 1258.023563, 1263.112215, 1268.200866, 1273.289517, 1278.378168, 1283.466820,
     1288.555471, 1293.644122, 1298.732773, 1303.821425, 1308.910076, 1313.998727, 1319.087378,
     1324.176030, 1329.264681, 1334.353332, 1339.441983, 1344.530635, 1349.619286, 1354.707937,
     1359.796588, 1364.885240, 1369.973891, 1375.062542, 1380.151193, 1385.239845, 1390.328496,
     1395.417147, 1400.505798, 1405.594450, 1410.683101, 1415.771752, 1420.860403, 1425.949055,
     1431.037706, 1436.126357, 1441.215008, 1446.303660, 1451.392311, 1456.480962, 1461.569613,
     1466.658265, 1471.746916, 1476.835567, 1481.924218, 1487.012870, 1492.101521, 1497.190172,
     1502.278823, 1507.367475, 1512.456126, 1517.544777, 1522.633428, 1527.722080, 1532.810731,
     1537.899382, 1542.988033, 1548.076685, 1553.165336, 1558.253987, 1563.342638, 1568.431290,
     1573.519941, 1578.608592, 1583.697243, 1588.785895, 1593.874546, 1598.963197, 1604.051848,
     1609.140500, 1614.229151, 1619.317802, 1624.406453, 1629.495105, 1634.583756, 1639.672407,
     1644.761058, 1649.849710, 1654.938361, 1660.027012, 1665.115663, 1670.204315, 1675.292966,
     1680.381617, 1685.470268, 1690.558920, 1695.647571];

lambda=round(lambdaRaa);
Energy = 10^9*hc*lambda.^-1;

for i = from:to
    Band = b(:, :, i);
    imshow(Band, []);
    title = ['Band:' ' '  num2str(i) ' ' num2str(lambda(i)) 'nm ' num2str(Energy(i), 3) 'eV'];

  % title(num2str(i));
     title(title);

  % M(i) = im2frame(Band);
     M(i) = getframe;

  pause(0.2);

end
movie2avi(M, 'cr1.avi', 'fps', 3);
end
```

3. Program used for converting HYSPEX to TIF

```
% Converting HYSPEX files to TIF files for use in ImageJ

% For MATLAB to read the filename, the function read_HYSPEX_file_all is used.
  Images = read_HYSPEX_file_all ('filename.hyspex.');

% Converting all 150 bands to TIF files
  for i=1:150
    if mod(i, 10) == 0 % Every tenth band == 15, to check that all bands are included
      disp ('OK')
    end
     All_images = (Images(:, :, i)-min(min(min(Images(:, :, i)))))/max(max(max(Images(:, :, i))));
     Filename = ['name_' num2str(i) '.tif'];
     imwrite (squeeze(All_images), Filename, 'tif');
  end
```

4. Program used for saving PCA results as TIF

```
% The path where the images are saved.
  datapath = '/Users/lena-mariejerpetjn/Desktop/Resuls - master/PCA/';
  X = read_HYSPEX_file_all ([datapath 'filename.hyspex']);

% # pixels in both x and y direction and # images (k) is found in the workspace window
  xim = reshape(name,:,:,k);
  xim_auto = xim.data;

% Loop used to save all images as TIF files.

  for i=1:k

    im1=xim_auto(:,:,i);

    max1=max(max(im1));
    min1=min(min(im1));

    im1=(im1-min1)/(max1-min1);

    imwrite(im1,['name' int2str(i) '.tif'])
  end
```

Appendix B

The recorded HYSPEX files used in this thesis

i. Hyspex files 300K

- *LM_180_romT_50000_us_HSNR04_2011-03-15T101611_corr.hyspex*

ii. Hyspex files 93 K

- *wafer180_fryst_50_motH_uglass_50000_us_HSNR04_2011-02-22T144221_corr.hyspex*
- *wafer180_fryst_50_uglass_50000_us_HSNR04_2011-02 22T153240_corr.hyspex*
- *180_220_190000_us_2011-03-04T141602_corr.hyspex*